

Remote sensing of turbid coastal and estuarine waters with VIIRS I (375 m) and M (750 m) bands

Quinten Vanhellemont^a, Ana Dogliotti^b, David Doxaran^c, Clémence Goyens^{a,d}, Kevin Ruddick^a and Dieter Vansteenwegen^e

^aOperational Directorate Natural Environments, Royal Belgian Institute of Natural Sciences, Brussels, Belgium; ^bInstituto de Astronomía y Física del Espacio (IAFE), CONICET-Universidad de Buenos Aires, Buenos Aires, Argentina; ^cLaboratoire d'Océanographie de Villefranche, CNRS-Sorbonne Université, Villefranche-Sur-Mer, France; ^dDepartment of Biology, Marine Optics and Remote Sensing (MarSens), Ghent University, Ghent, Belgium; ^eInfrastructure Department, Flanders Marine Institute (VLIZ), Ostend, Belgium

ABSTRACT

The Visible Infrared Imaging Radiometer Suite (VIIRS) is a visible, near and shortwave, to thermal infrared multispectral scanning instrument operational on three polar orbiting satellites, Suomi-NPP, JPSS-1, and JPSS-2. In the present paper, the processing of VIIRS using ACOLITE is introduced, using the Dark Spectrum Fitting (DSF) algorithm for processing of the visible to shortwave infrared bands. ACOLITE now includes support for processing both the imaging (I) and moderate (M) resolution bands at 375 m and 750 m spatial resolution, respectively. In most conditions encountered in the present study, the SWIR bands (either I or M) are automatically selected by the DSF for performing the aerosol correction. The processing is evaluated for turbid water remote sensing via autonomous hyperspectral radiometry from four sites across coastal and estuarine waters: two sites in Belgium and one each in France and Argentina. Through analysis of hundreds of matchups between the satellite and in situ measurements, a generally good performance is found for both I and M bands, especially for bands with the largest water signal, i.e. bands between 490 and 670 nm, where on average relative differences of 10–15% were found. Reflectance biases are generally less than 0.01, with a negative sign in the green and red bands and a positive sign in the blue and NIR bands. Similar matchup results are found for the I and M red and NIR bands, with a slightly higher scatter for the NIR bands. An additional comparison with OCSSW/I2gen processing of the M band data is performed for various configurations. Overall, DSF performance is better in the visible bands, whereas I2gen outputs are more closely aligned with the in situ measurements in the NIR. On average, negative biases are found for all I2gen configurations, up to –0.02 in the blue bands. Using either the SWIR1 + 2 or SWIR1 + 3 bands for the aerosol correction gives the best performance for I2gen processing. For the three VIIRS instruments separately, the average


ARTICLE HISTORY

Received 18 March 2024
Accepted 5 September 2024

KEYWORDS

VIIRS; ACOLITE; I2gen; atmospheric correction; aquatic applications; turbid waters; hyperspectral

CONTACT Quinten Vanhellemont  quinten.vanhellemont@naturalsciences.be  Royal Belgian Institute of Natural Sciences, Operational Directorate Natural Environments, Vautierstraat 29, Brussels 1000, Belgium

 Supplemental data for this article can be accessed online at <https://doi.org/10.1080/01431161.2024.2407559>

© 2024 The Author(s). Published by Informa UK Limited, trading as Taylor & Francis Group.

This is an Open Access article distributed under the terms of the Creative Commons Attribution License (<http://creativecommons.org/licenses/by/4.0/>), which permits unrestricted use, distribution, and reproduction in any medium, provided the original work is properly cited. The terms on which this article has been published allow the posting of the Accepted Manuscript in a repository by the author(s) or with their consent.

spectral differences with in situ measurements are comparable, with the most important deviation occurring at the Suomi-NPP shortest blue bands, where DSF processing gives a larger positive bias, up to nearly 0.02. For these bands, results from I2gen correspond more closely across the three instruments – although with significant negative biases for all three sensors up to -0.02 – presumably due to the use of system vicarious calibration gains in that processor. An operational network of autonomous hyperspectral instruments provides validation data for any overpassing optical imaging satellite in its commissioning or operational phase and eliminates the need for spectral interpolation or band shifting. In the case of VIIRS specifically, the hyperspectral instruments provide adequate data for the validation of the 20, 40 and 80 nm wide bands. With three operational wide-swath instruments, which provide largely interoperable data, a high frequency of observations is available, especially for study areas at higher latitudes. The novel exploitation of the I bands is now possible, thanks to the free and open source availability of ACOLITE. The advantage of the higher resolution I band data, combined with multiple VIIRS overpasses per day, is demonstrated for mapping turbidity in nearshore regions with high spatial variability and for detecting under-resolved floating algae.

HIGHLIGHTS

- The open-source ACOLITE processor was adapted for VIIRS I (375 m) and M (750 m) data
- Three operational VIIRS (Suomi-NPP, JPSS-1 and JPSS-2) were processed and validated
- In situ autonomous hyperspectral radiometry was used for performance evaluation
- ACOLITE I and M band outputs compared well across hundreds of turbid water matchups
- Turbidity and FAI product resolution were improved with ACOLITE I bandprocessing

1. Introduction

The Visible Infrared Imaging Radiometer Suite (VIIRS) was first launched in 2012 on the joint NASA/NOAA Suomi National Polar-orbiting Partnership (Suomi-NPP) and subsequently in 2017 and 2022 on two Joint Polar Satellite System satellites (JPSS-1 and JPSS-2, renamed NOAA-20 and NOAA-21 after launch). JPSS-2/NOAA-21 has been handed over by NASA to NOAA on 30 March 2023 and was officially declared operational on 8 November 2023. Two future VIIRS sensors are planned on two follow-up JPSS/NOAA satellites. VIIRS has 22 spectral bands, with a nominal spatial resolution of 375 m in the 5 imaging 'I' bands and 750 m in 16 moderate resolution 'M' bands and in the sensitive day/night panchromatic band (DNB). The 5 I bands cover the red, near-, shortwave-, medium-, and longwave infrared, and the M bands cover the visible from 412 nm to longwave infrared up to 12.5 μm .

Since the launch of Suomi-NPP, VIIRS M band data have been used for ocean colour purposes alongside other missions such as the Moderate Resolution Imaging Spectroradiometer (MODIS) on board of the Aqua and Terra satellites and the Ocean

and Land Colour Imager (OLCI) on board Sentinel-3 A and B, or to extend data records from defunct missions such as the Sea-viewing Wide Field-of-view Sensor (SeaWiFS) and Medium Resolution Imaging Spectrometer (MERIS). VIIRS M band data were used for mapping of water turbidity (Balasubramanian et al. 2020; Novoa et al. 2017), in multi-mission analyses of remote sensing reflectance in matchup (Barnes et al. 2019; Hlaing et al. 2013), or as long term time-series with their derived chlorophyll a concentration, for example, in the Ocean Colour Climate Change Initiative (Mélin et al. 2017; Sathyendranath et al. 2019)

Similar to the first two I bands on VIIRS, MODIS has two 'high resolution' bands at 250 m covering red and NIR wavelengths. Applications of these bands arrived rather soon after the operational distribution of MODIS products, for example, for retrieving coastal and estuarine water turbidity products (Chen, Hu, and Muller-Karger 2007; Doxaran et al. 2009; Franz et al. 2006; Miller and McKee 2004). Various authors have shown interest in the VIIRS I bands for mapping of coastal waters, e.g. for turbidity retrieval (Novoa et al. 2017) or mapping of floating algae (Hu 2009; Qi et al. 2020), or have applied statistical methods for sharpening VIIRS M data to I resolution (Liu and Wang 2020; Vandermeulen et al. 2015). However, the VIIRS I bands have in general been much less used for aquatic applications compared to the MODIS 250 m bands, presumably because the former cannot be processed by open source SeaDAS OCSSW/I2gen or any other freely available processor. The atmospheric correction of the Suomi-NPP/VIIRS red imaging band (I01) has been previously demonstrated by Wang and Jiang (2018) using the NOAA MSL12 operational processor. The authors found good correspondence between the spectrally close red I and M bands, as well as for four matchups with in situ data. They did not include the NIR imaging band (I02), which may provide useful observations in extremely turbid waters, e.g. in the case of red band reflectance saturation (Luo et al. 2018). The NOAA MSL12 processor is unfortunately not available to the public, and hence, there has been little use of VIIRS I band data. Level 2 data from the red I band as processed with MSL12 are distributed through the NOAA CoastWatch data portal (<https://coastwatch.noaa.gov/cwn/index.html>, accessed 19 August 2023), but they are averaged to the resolution of the M bands.

In the current paper, the processing with ACOLITE/DSF of both I and M data from the three currently operating VIIRS satellite sensors is presented. A matchup analysis is performed with hundreds of measurements from autonomous hyperspectral radiometers installed at four sites in some of the world's most turbid coastal and estuarine waters. Additionally, the performance of the OCSSW/I2gen processor for the M bands as provided by the Ocean Biology Processing Group (OBPG) at NASA Goddard is evaluated. A limited number of demonstration applications using the I bands is provided. ACOLITE processing software is freely available under an open source licence, now updated to enable public use of the VIIRS I and M band data archive.

2. Data and methods

2.1. Satellite data

VIIRS is a multispectral whiskbroom scanning imager with 22 spectral bands covering the visible to thermal infrared across three band sets. Its nadir spatial resolution is nominally

375 m in the five imaging (I) bands and 750 m in the 16 moderate (M) resolution bands and the one day-night-band (DNB). With a wide swath of 3060 km, a single sensor can provide daily coverage of the globe, albeit at a reduced spatial resolution at higher viewing zenith angles. The bow-tie effect that occurs when observing off-nadir pixels is reduced for VIIRS compared to MODIS by the use of rectangular detectors smaller than the nominal pixel size and a pixel aggregation procedure (Wolfe et al. 2013). The detectors are oriented with their smaller dimension in the along-scan direction, and individual VIIRS pixels are aggregated from 3×1 , 2×1 , or 1×1 detectors at the nadir, middle, and edge of scan. For bandwidth reasons, VIIRS off-nadir coverage is additionally reduced by an on-board trim procedure when scans overlap by several pixels, resulting in apparent gaps in the top-of-atmosphere scan data. This procedure reduces, but does not eliminate, pixel overlap at higher observation angles, and the resulting scan data need to be reprojected before use. An overview of I and M bands covering the visible to shortwave infrared (VSWIR) wavelengths used in the present paper is provided in Table 1. The relative spectral response of these bands is provided in Supplementary Material 1. The M bands are typically around 20 nm wide in the visible wavelength range, with varying width in the NIR and SWIR (up to 60 nm). The spectral width and response of the I02/M07 and I03/M10 band pairs are well aligned, while the I01 band is much wider (80 nm) compared to the corresponding M05 band (20 nm).

Imagery recorded by VIIRS on board of Suomi-NPP, JPSS-1, and JPSS-2 was obtained as uncalibrated top-of-atmosphere scans in digital counts at Level-1A (L1A) from OBP. L1A data were processed using the SeaDAS processing components (OCSSW, <https://seadas.gsfc.nasa.gov/downloads/>, accessed 24 April 2023) version V2023.2 to generate geolocation files (GEO) and calibrated top-of-atmosphere radiances at Level-1B (L1B) for both the I and M bands in the NetCDF format. The DNB data cannot be calibrated with OCSSW and are hence not used. These GEO and L1B files are the required input files for further processing with OCSSW I2gen and ACOLITE (see section 2.2).

Table 1. VIIRS VSWIR band information. I and M bands have nominal resolutions of 375 m and 750 m, respectively. The last three columns provide the band- and sensor-specific suffix for the bands within the ACOLITE outputs. Information obtained from NOAA technical report NESDIS 142 (<https://ncc.nesdis.noaa.gov/documents/documentation/viirs-users-guide-tech-report-142a-v1.3.pdf>, accessed 21 July 2023). Thermal infrared (TIR) bands (I04, I05, M12, M13, M14, M15 and M16) and the DNB were omitted, as they are not used in the present paper.

| Band | Wavelength | Suomi-NPP | JPSS-1 | JPSS-2 |
|------|---------------------------|-----------|----------|----------|
| I01 | 0.600–0.680 μm | I01_638 | I01_643 | I01_642 |
| I02 | 0.846–0.885 μm | I02_862 | I02_867 | I02_868 |
| I03 | 1.580–1.640 μm | I03_1601 | I03_1604 | I03_1614 |
| M01 | 0.402–0.422 μm | M01_411 | M01_411 | M01_411 |
| M02 | 0.436–0.454 μm | M02_444 | M02_445 | M02_445 |
| M03 | 0.478–0.498 μm | M03_486 | M03_489 | M03_489 |
| M04 | 0.545–0.565 μm | M04_551 | M04_557 | M04_555 |
| M05 | 0.662–0.682 μm | M05_671 | M05_667 | M05_672 |
| M06 | 0.739–0.754 μm | M06_745 | M06_746 | M06_747 |
| M07 | 0.846–0.885 μm | M07_862 | M07_868 | M07_868 |
| M08 | 1.230–1.250 μm | M08_1238 | M08_1239 | M08_1241 |
| M09 | 1.371–1.386 μm | M09_1375 | M09_1375 | M09_1382 |
| M10 | 1.580–1.640 μm | M10_1602 | M10_1604 | M10_1614 |
| M11 | 2.225–2.275 μm | M11_2257 | M11_2259 | M11_2252 |

GEO and L1B data are also processed and distributed in a compatible format by the Level-1 and Atmosphere Archive & Distribution System Distributed Active Archive Center (LAADS-DAAC), provided through the EarthData Search Portal (<https://search.earthdata.nasa.gov/search/>, accessed 24 April 2023). These products have the advantage that they do not require installation of the OCSSW package and running of the VIIRS geolocation and calibration tools. These data have identifiers VNP02MOD, VJ102MOD, and VJ202MOD for M band radiance (i.e. labelled '02') and VNP03MOD, VJ103MOD, and VJ203MOD for M band geolocation (i.e. labelled '03') for Suomi-NPP, JPSS-1 and JPSS-2, respectively. For the I bands, the data identifiers are VNP02IMG, VJ102IMG and VJ202IMG and VNP03IMG, VJ103IMG and VJ203IMG.

2.2. Atmospheric correction

The VIIRS L1B imagery in NetCDF format was processed using two atmospheric correction software packages: ACOLITE (<https://github.com/acolite/acolite>, accessed 20 August 2023) and OCSSW I2gen (see previous section). ACOLITE requires either two or four inputfiles for processing a VIIRS scene, i.e. the GEO and L1B for either or both the I and M bands, while I2gen uses only the two M band GEO and L1B files. Images were subset to an approximately 36×36 km region of interest over the validation sites (see further), which gives a reasonable extent to fix the aerosol optical thickness (Vanhellemont and Ruddick 2021).

For the present study, ACOLITE was adapted for VIIRS L1B data processing using files either output by OCSSW or obtained from the LAADS-DAAC. ACOLITE includes the Dark Spectrum Fitting (DSF) algorithm for atmospheric correction of VSWIR data (Vanhellemont 2019; Vanhellemont and Ruddick 2018) and the Thermal Atmospheric Correction Tool (TACT) for processing of TIR data (bands I04, I05, M12, M13, M14, M15 and M16). The evaluation of the latter is out of the scope of the present paper and will be performed at a later stage. Processing of either M or I or both M and I bands is supported by ACOLITE, with all bands processed at either I or M band resolution. Pixels are either replicated or mean-averaged to create finer or coarser resolution data, i.e. M band data are repeated four times to make up four pixels at the I band resolution, and four I band pixels are averaged to make up a single pixel at the M band resolution. This option can be specified by setting 'viirs_option' to either a combination of the elements 'mod' for the M bands and 'img' for the I bands separated by a plus sign, i.e. 'mod', 'img', 'mod+img', and 'img+mod'. The first (or only) element defines the output resolution, and the output band set depends on the specified element(s). In the present paper, 'viirs_option=img+mod' is evaluated, i.e. both I and M band data are processed at 375 m resolution. VIIRS L1B data were (1) cropped to the study area along the nearest complete scan line (i.e. in sets of 16 M or 32 I along-track pixels), in order to perform a consistent scan reprojection; (2) converted from top-of-atmosphere radiance (L_t) to top-of-atmosphere reflectance (ρ_t) using the provided scale and offset data, and the per-pixel cosine of the sun zenith angle, assuming level terrain; and (3) stored in a generic ACOLITE 'Level 1 Reflectance' (L1R) NetCDF file. The VIIRS L1B quality layer for each band was used to mask pixels when flags were set for 'Saturation', 'Temp_not_Nominal', 'Missing_EV', 'Cal_Fail', 'Dead_Detector', and 'Noisy_Detector', i.e. when the binary AND with the sum of flag values 4, 8, 512, 1024, 2048, and 4096 was non-zero.

ACOLITE/DSF was used for processing of the reprojected (see the next section) generic L1R file, using two configurations with a single aerosol type and optical thickness (τ_a), defined at 550 nm, estimated over the study site subset: (1) without ('DSF') and (2) with ('DSF+GC') per-pixel SWIR-based glint correction (Harmel et al. 2018; Vanhellemont 2019). In this configuration of DSF processing, a dark spectrum (ρ_{dark}) is constructed based on the darkest observed ρ_t in each band across the image subset. The ρ_{dark} is assumed to have zero surface level reflectance ($\rho_s = 0$), and hence for each band, under the specific observation and illumination geometry, τ_a can be estimated for a given aerosol model by interpolation of modeled atmospheric path reflectance (ρ_{path}) from precomputed lookup tables generated using 6 SV (Kotchenova et al. 2006; Vanhellemont 2020). This procedure provides a spectrum of estimated τ_a (at 550 nm) in each band, and for further processing, the lowest τ_a is used to avoid negative retrievals in the other bands (Vanhellemont and Ruddick 2018). A final selection between aerosol models is performed based on the fit between the observed ρ_{dark} and the modeled ρ_{path} in the two best fitting bands for each model. Further details on DSF processing can be found in supporting open access publications, e.g. Vanhellemont and Ruddick (2018, 2021); Vanhellemont (2019, 2020). The glint correction assumes that the residual SWIR signal after atmospheric correction can be attributed fully to sun glint. The SWIR band giving the lowest glint reflectance is used as the reference band, and the observed glint signal is then extrapolated to the visible and NIR bands by taking into account the atmospheric transmittance and Fresnel reflectance ratios in the reference and target bands. Two additional configurations were also evaluated, i.e. the application of the DSF τ_a estimation per-pixel, without ('DSFR') and with ('DSFR+GC') the per-pixel glint correction. In this configuration, the DSF process as described above is performed on an individual pixel basis rather than across an image subset. In the interest of improving the processing speed, a reverse lookup table was constructed to directly interpolate ρ_{path} to τ_a . Other atmospheric correction parameters are then interpolated from the selected τ_a using the regular lookup tables. ACOLITE outputs were masked to exclude non-water pixels using a series of tests. Pixels were masked using thresholds on the top-of-atmosphere reflectance, i.e. when (1) $\rho_t > 0.3$ in any VSWIR band, (2) $\rho_t > 0.005$ in the M9 cirrus band, or (3) $\rho_t > 0.0215$ in the M10 band at around $1.6 \mu m$. Additional masking was performed for mixed pixels that can be identified by the resolution differences of I and M bands, i.e. pixels were masked when the absolute difference in ρ_t between the two $1.6 \mu m$ bands (I03 and M10) was > 0.002 or when the relative difference was $> 20\%$.

OCSSW/l2gen was used to process the VIIRS M data using four configurations: (1) the standard processing using the two NIR bands M06 and M07 for the aerosol correction ('l2gen STD') and three SWIR-based processing configurations using channels (2) SWIR1 and SWIR2 ('l2gen SWIR1 + 2'), (3) SWIR1 and SWIR3 ('l2gen SWIR1 + 3'), and (4) SWIR2 and SWIR3 ('l2gen SWIR2 + 3') for the multiple scattering aerosol estimation, where SWIR1 is M08 at $1.2 \mu m$, SWIR2 is M10 at $1.6 \mu m$, and SWIR3 is M11 at $2.2 \mu m$. As the study sites all have turbid to extremely turbid waters, the blue-to-green ratio chlorophyll a retrieval-based bidirectional reflectance distribution function correction (BDRF) was disabled ('brdf_opt = 0') as were the masking of high radiance ('maskhilt = 0') and stray light pixels ('maskstlight = 0') for all l2gen configurations. The cloud masking threshold was set to 0.018 on the SWIR3 band. An additional variation of these four

settings was examined by switching the aerosol correction mode from the default multiple scattering, relative humidity-based aerosol models (Ahmad et al. 2010), with iterative NIR correction ('aeropt = -17') to the simple two-band multiple scattering aerosol model selection ('aeropt = -1'). In essence, this variation more closely resembles the original Gordon and Wang (1994) method, as it disables the iterative NIR correction (Bailey, Franz, and Jeremy Werdell 2010), which is based on a blue-to-green ratio of chlorophyll a retrieval that may not be applicable in waters dominated by non-algal particulate scattering. ρ_w was computed from the I2gen outputs as $\pi \times Rrs$.

2.3. Swath reprojection

The L1R files were reprojected to a Universal Transverse Mercator (UTM) projection with 375×375 m pixel sizes before ACOLITE/DSF processing using bilinear interpolation and averaging multiple overlapping observations in the off-nadir area affected by the bow-tie effect. If residual scan line gaps were present in the output product, pixels were filled via bilinear interpolation. ACOLITE always crops the VIIRS data along the nearest bounding scan line edge, and the reprojection is performed per scan line of either 16 or 32 pixels for the M and I band resolutions. An example of the bow-tie effect and reprojected data is shown in Figure 1. OCSSW/I2gen processing outputs were cropped and reprojected using the same method. The different order of the reprojection step, i.e. before (ACOLITE) and after (I2gen) processing, was chosen for technical reasons. The DSF with a fixed aerosol optical thickness retrieval relies on using information from the subscene, and the reprojection before processing ensures that each location has the same weight in this estimation. Only minor differences were found between the application of the reprojection before or after ACOLITE/DSF processing (not shown), and the order of reprojection is not deemed to have important consequences for the current application. However, reprojection at the L1R level has a processing time advantage as less datasets need to be reprojected, i.e. only ρ_t for VSWIR and L_t for the TIR bands. The I2gen processing does not support reprojection before or during processing, so it was done afterwards. For the extraction of matchups, there are several problems using unprojected data, e.g. pixel overlap, geolocation replication, and presence of scan line gaps.

2.4. In situ data

In situ measurements from two autonomous hyperspectral radiometer systems were used, i.e. the pan-and-tilt hyperspectral radiometer system (PANTHYR, Vansteenwegen et al. (2019)), and the hyperspectral pointable system for terrestrial and aquatic radiometry (HYPSTAR®). The PANTHYR uses a pair of TriOS RAMSES instruments, one for radiance and one for irradiance, and measures in 190 channels between 320 and 950 nm with a full width at half maximum (FWHM) of about 10 nm, with a usable range of about 400–900 nm. The HYPSTAR® Standard Range instrument (HYPSTAR®-SR) was used, which has a visible to near-infrared sensor measuring in 1330 channels between 380 and 1000 nm (FWHM of 3 nm). One PANTHYR instrument was deployed on the Blue Accelerator Platform (callsign RT1) near Oostende, Belgium, site name O1BE. This deployment has been previously used in turbid water validation studies, e.g. for the Ocean and Land Colour Instrument (OLCI) on Sentinel-3 (Vanhellemont and Ruddick 2021) and

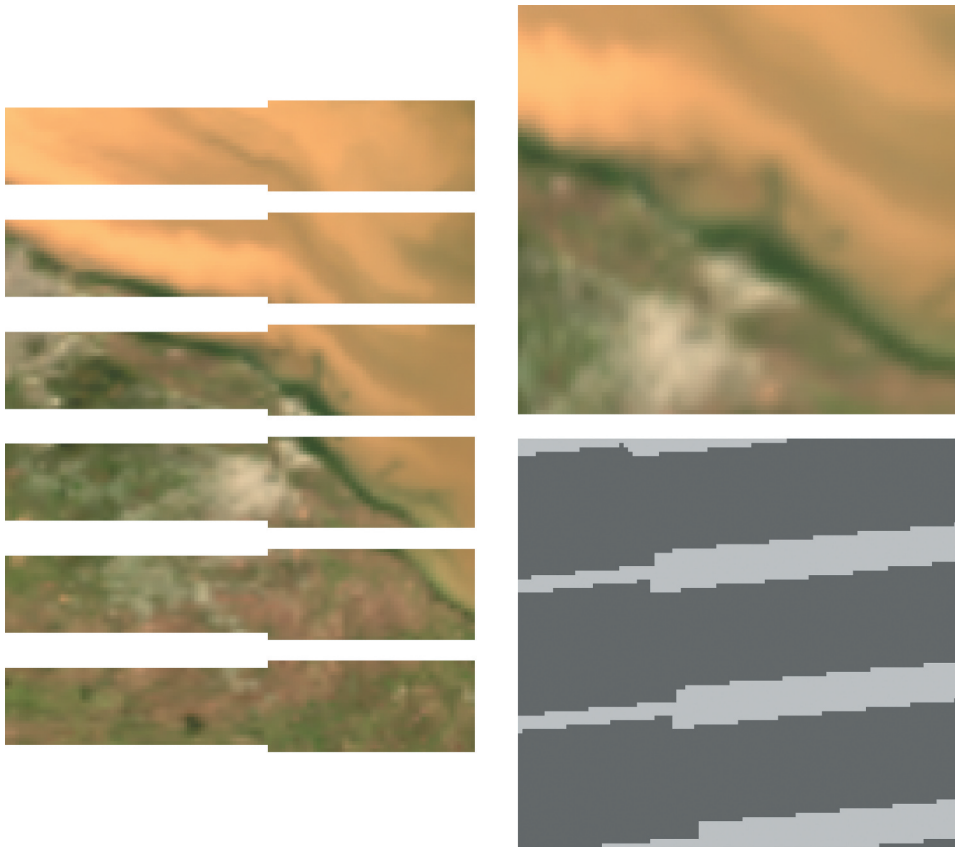


Figure 1. Example of the scan line gaps caused by on-board pixel deletion in a subset of a JPSS-2/VIIRS image taken 2023-04-29 17:03 UTC over the LPAR site, with an unprojected ρ_s RGB (665, 560 and 490 nm) on the left. Note the transition between 1 x 1 and 2 x 1 detector aggregation in the middle of the image, i.e. where the gap reduces in width, and the repeated observation of certain targets near the gaps as a result of the bow-tie effect. The transition from 2 x 1 to 3 x 1 detector aggregation further east closes the gap. The top right panel shows the reprojection to the 36 x 36 km UTM grid, and the bottom right panel indicates which pixels were mean-averaged for the I01 band. Targets were either observed once (dark shading) or twice (light shading). Latitude and longitude annotations are suppressed for legibility and can in fact not be displayed for unprojected data. The extents are the same as in Figures 3 and 10.

SuperDove cubesats (Vanhellemont 2023). Three HYPSTAR® instruments were deployed, one at the Río de la Plata estuary, near La Plata, Argentina, site name LPAR (2); the Gironde estuary mouth, near Le-Verdon-Sur-Mer, France, site name MAFR; and (3) the MOW1 platform near Zeebrugge, Belgium, site name M1BE. An overview of sites and data availability per deployment is given in Table 2, and site locations are illustrated with Sentinel-2 imagery in Figure 2.

Both in situ systems are mounted on a pan and tilt head and measured with similar protocols, i.e. using a nadir viewing angle of 40°, at 90°, 135°, 225° and 270° relative azimuth angles ($\delta\phi$) to the sun to minimise sky and sun reflectance on the air–water interface (Mobley 1999; K. G. Ruddick et al. 2006). A measurement cycle consists of sequential measurements of downwelling irradiance (E_d , three replicates), downwelling

Table 2. Study site details with instrument, deployment and matchup locations. The turbidity range at the site was derived from the in situ reflectance data and the algorithm of Nechad, Ruddick, and Neukermans (2009).

| Site | O1BE | LPAR | MAFR | M1BE |
|--------------|----------------|---|----------------|---------------|
| Instrument | PANTHYR | HYPSTAR | HYPSTAR | HYPSTAR |
| Latitude | 51.24642N | 34.81780S | 45.54794N | 51.36055N |
| Longitude | 2.91993E | 57.89607W | 1.03963W | 3.11825E |
| Matchup Lat. | 51.24883N | 34.80920S | 45.55058N | 51.36008N |
| Matchup Lon. | 2.91224E | 57.89515W | 1.03188W | 3.11670E |
| Deployments | 12/2019–8/2020 | 12/2021–9/2022 9/2021–11/2022 4/2023–7/2023 | 12/2021–4/2023 | 2/2023–4/2023 |
| Turbidity | 2–80 FNU | 8–180 FNU | 3–160 FNU | 6–90 FNU |

radiance (L_d , three replicates), upwelling radiance (L_u , eleven replicates for PANTHYR, six for HYPSTAR[®]) and three more replicates of L_d and E_d after the L_u measurements. Data from a cycle that pass quality control are mean-averaged, and if sufficient replicates are available, i.e. 5/6 E_d , 5/6 L_d and 9/11 L_u for PANTHYR, as well as at least 3 replicates of each parameter for HYPSTAR[®], the water-leaving radiance reflectance (ρ_w) is computed by:

$$\rho_w = \frac{\pi \cdot L_w}{E_d}, \quad (1)$$

where L_w is the water-leaving radiance, computed from the L_u and L_d average measurements:

$$L_w = L_u - \rho_f \cdot L_d, \quad (2)$$

where ρ_f is the effective Fresnel reflectance factor, as estimated from lookup tables provided by Mobley (1999). Wind speed for interpolation of the lookup tables is obtained as the nowcast wind speed from the Global Data Assimilation System (GDAS) as provided by National Centers for Environmental Information (NCEI, dataset identifiers NCEI DSI 6172 and gov.noaa.ncdc:C00379) for PANTHYR processing. HYPSTAR[®] data were processed with a fixed 2 m/s wind speed for MAFR and M1BE and using variable wind speed for LPAR derived from NCEP/MET data obtained from the oceandata server of the OBPG. Further details on in situ data processing can be found in Vansteenwegen et al. (2019); Vanhellemont (2020) for PANTHYR and in De Vis et al. (2024) for HYPSTAR[®].

Per site, data from a single $\delta\phi$ were used, depending on the data availability and matchup potential with VIIRS overpass times. The $\delta\phi$ depended on the site specific installation and characteristics: O1BE and LPAR were measured at 270°, MAFR at 135°, and M1BE at 90°. For MAFR, an additional filtering on the in situ data as provided on Zenodo was performed, rejecting data with a sun zenith angle θ_s of $>60^\circ$ to avoid measurement of the platform shadow at $\delta\phi$ of 135° in cases of low sun elevation.

2.5. Matchups and quality control

Matchup data were extracted as 3×3 pixel boxes from the 375×375 m UTM projected data, centred on a reference location for each site (Table 2), retaining the matchup if at least three out of nine pixels were not masked in the processor masking procedure. The reference locations were chosen one to three pixels away

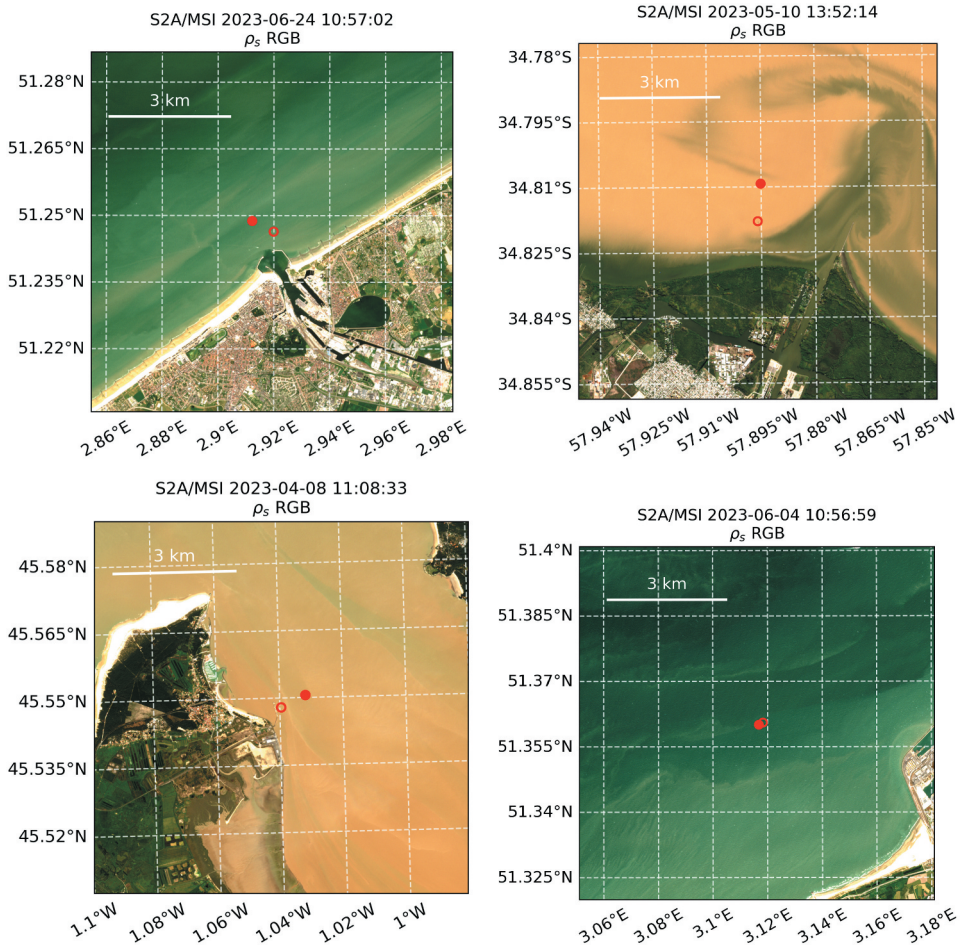


Figure 2. Sentinel-2A imagery subsets (about 9 x 9 km) ρ_s RGB (665, 560 and 490 nm) composites over the instrument deployment locations: O1BE (top left, 2023-06-24), LPAR (top right, 2023-05-10), MAFR (bottom left, 2023-04-08) and M1BE (bottom right, 2023-06-04). The open circle denotes the deployment location, and the closed circle denotes the reference location at the centre of a pixel in the output UTM grid. Decimal coordinates of these points are provided in Table 2. Contains modified Copernicus sentinel data [2023].

in the UTM projection of the final output data to avoid on one hand the contamination of land and mixed land/water pixels as a result of the very near-shore position of the measurement stations, which is increased at higher viewing angles by growing pixel sizes and scan line overlap. The reference pixels were chosen considering typical masking results for VIIRS reprojected data, and their location is represented by the centre of the pixel in the UTM grid (Table 2). This rather relaxed pixel masking criterion was applied (i.e. using matchups with $\geq 3/9$ valid pixels) to allow for matching up with the sites very close to the land, i.e. close to consistently masked data. Matchups were retained if an in situ measurement was available within 30 minutes of the satellite overpass time. If bounding measurements were available each within 30 minutes of the overpass time, they were linearly interpolated to the overpass time. Matchups were evaluated per band according to three

subsets, i.e. considering valid data (1) per processor, (2) for common data across processors in the current band, and (3) for common data where all processors provide a full spectrum.

Statistics were computed per processor for each matchup subset and separately per satellite and per site. A Reduced Major Axis (RMA) regression, i.e. the line bisecting two Ordinary Least Squares (OLS) regressions swapping both compared datasets, was performed per band. Average statistics were computed between in situ (x) and satellite (y) data: the Mean Difference (MD), representing the bias,

$$MD = \sum_{i=1}^n \frac{y_i - x_i}{n}, \quad (3)$$

the Root Mean Square Difference (RMSD), representing the scatter,

$$RMSD = \sqrt{\sum_{i=1}^n \frac{(y_i - x_i)^2}{n}}, \quad (4)$$

and the Mean Absolute Percentage Difference (MAPD), representing the relative difference,

$$MAPD = \sum_{i=1}^n \left| \frac{y_i - x_i}{0.5 \cdot (y_i + x_i) \cdot n} \right|. \quad (5)$$

3. Results

Example matchups and RGB composites are provided in [Figure 3](#), one from each satellite sensor. The example from LPAR (top) illustrates a fairly typical result at the site, with all l2gen configurations underestimating across the spectrum and a rather good match for ACOLITE/DSF. A mismatch in the spectral shape in the shortest two bands (M01 and M02) can be observed for ACOLITE/DSF in the case of this Suomi-NPP matchup. A low difference is found between DSF and DSF+GC as a low SWIR signal was observed in this westward looking subscene, and hence, almost no glint signal is present and removed. Two examples from JPSS-1 and JPSS-2 are provided for O1BE, one atypical with all processors give a very similar result (middle), and one more typical (bottom), where l2gen provides a rather good fit in the NIR but tends to underestimate in the VIS. The standard l2gen processing gives the largest underestimation in the VIS. ACOLITE/DSF tends to overestimate slightly in the NIR, but has a close fitting result in the VIS. A slight increase in the shortest blue band (M01) can be seen in the ACOLITE/DSF result for JPSS-2.

In total, ACOLITE/DSF (without and with glint correction) using a single τ_a estimate over the subscene provided 389 matchups across the four sites, i.e. O1BE ($n = 219$), LPAR ($n = 124$), MAFR ($n = 32$), M1BE ($n = 14$) and three satellite sensors, i.e. Suomi-NPP ($n = 149$), JPSS-1 ($n = 218$) and JPSS-2 ($n = 22$). For these matchups, the DSF automatically selected predominantly the SWIR bands ($n = 356$, 91%) for τ_a determination. The SWIR band use was distributed about evenly across the four I03, M08, M10, and M11 bands. The VIS ($n = 23$, 6%) and NIR ($n = 10$, 3%) band use was limited to about 9% of the matchups and was constrained mainly to the blue (M01) and NIR bands (I02, M06). The average τ_a determined by the DSF across the matchups was 0.12 (at 550 nm), with a standard

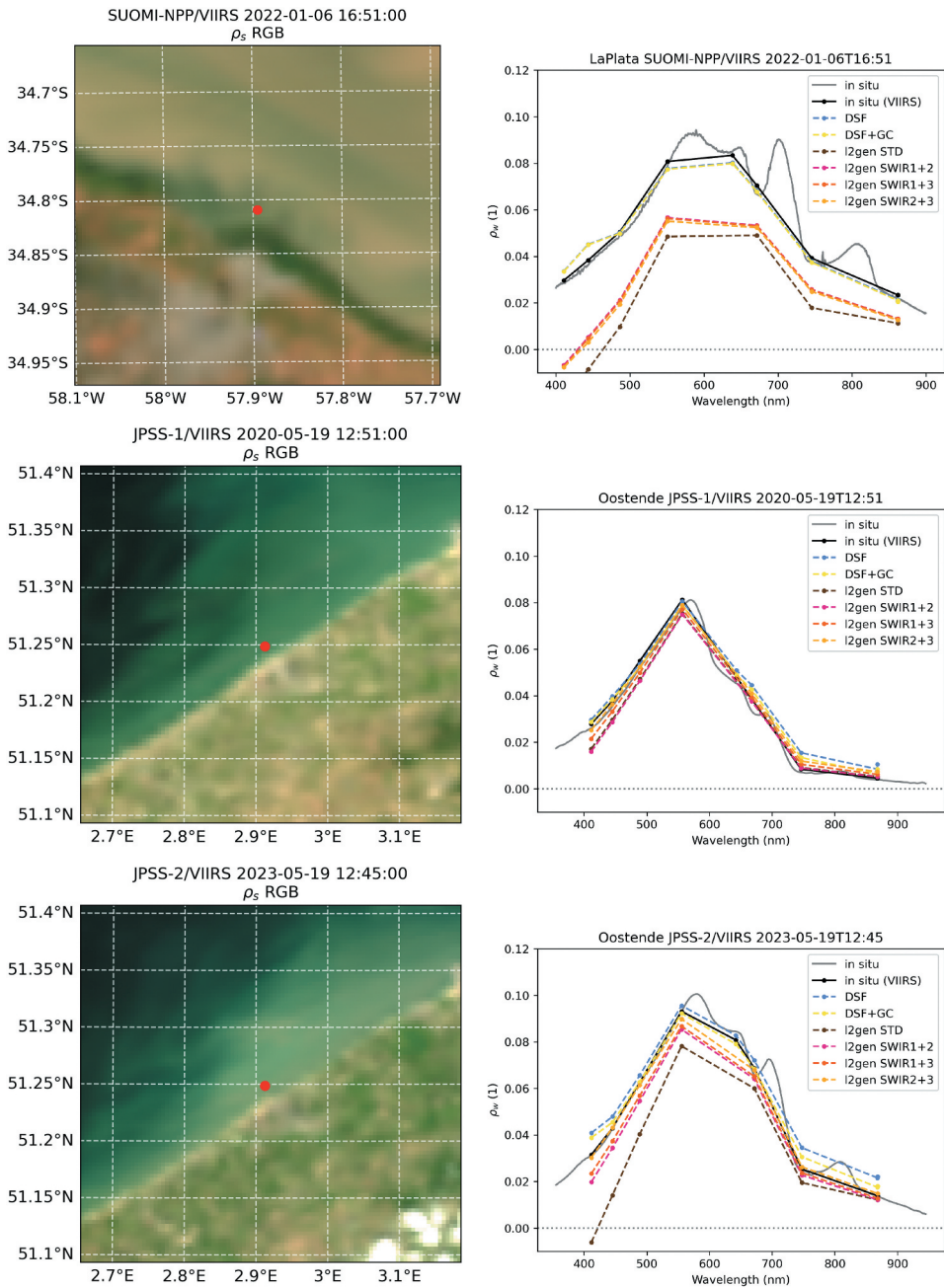


Figure 3. Example matchups between VIIRS and in situ data showing the ρ_s RGB composite of the 36 x 36 km subsense centred on the in situ measurement location (left) and spectral plot (right). The circle on the RGB composite shows the matchup reference location. The dots connected by a solid black line represent the in situ measurement resampled to the VIIRS bands, and the dots connected by coloured dashed lines represent the satellite measurement. Note the extra point for the red I band around 640 nm in the in situ and ACOLITE spectra. The ACOLITE NIR I band points overlap with the NIR M band. Top: Suomi-NPP for the LPAR site (2022-01-11, 16:57 UTC), middle and bottom: JPSS-1 (2020-05-19, 12:51 UTC), and JPSS-2 (2023-05-19; 12:45 UTC) for the O1BE site.

deviation of 0.08. A second band is used in the DSF to determine the best fitting aerosol model, where again predominantly the SWIR bands were used ($n = 363$, 93%); in this case, mainly the SWIR at $1.6 \mu\text{m}$, i.e. I03 ($n = 150$, 38%) and M10 ($n = 126$, 32%). Two aerosol models were included in ACOLITE, i.e. the continental ‘model 1’ and maritime ‘model 2’ as implemented in 6 SV, which were selected for 30% and 70% of the matchups, respectively. Including the glint correction (ACOLITE/DSF+GC) reduced the retrieved reflectances only slightly in the present dataset, as most severely glinted pixels will have been masked out by the automated masking. The largest impact of the glint correction can be observed in the NIR bands. Scatter plots for the red and NIR I bands for all three VIIRS instruments combined are provided in Figure 4 for the single τ_a results without and with the glint correction. Outliers in these plots are caused by either spatial variability of turbidity between the site and reference locations, or clouds and cloud shadows not detected by

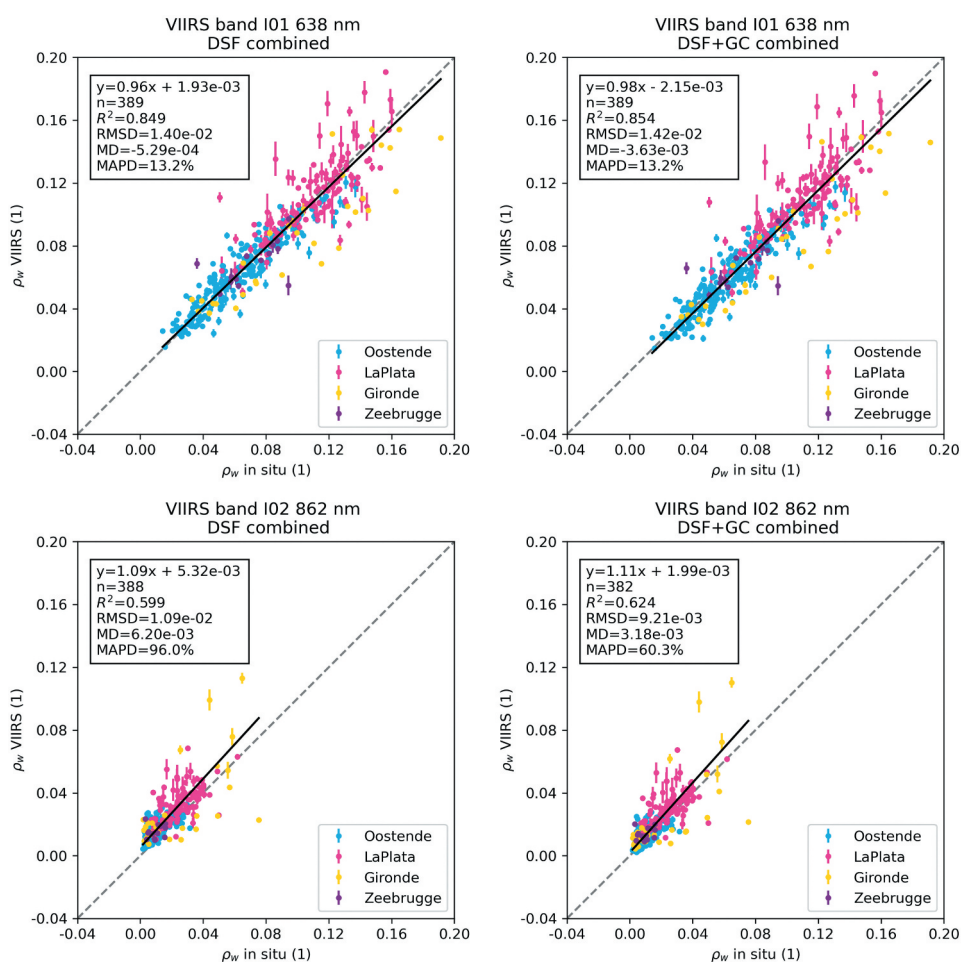


Figure 4. Matchups with in situ measurements of the I bands on VIIRS as processed with ACOLITE/DSF using a single τ_a estimate over the 36×36 km subscene. The top and bottom rows show the I01 (red) and I02 (NIR) bands. The left column has the per-pixel SWIR based glint correction disabled, and the right column has it enabled. Wavelengths in the title were taken from Suomi-NPP. Points represent the mean, and the vertical error bars represent the standard deviation in the 3×3 pixel box.

the masking procedure. These are not filtered out to represent typical satellite data use and to highlight that improvements are needed for satellite data masking procedures. A full series of scatter plots for DSF and DSF+GC is provided in Supplementary Material 2. The results for the per-pixel τ_a estimation, i.e. the resolved DSF (DSFR), gave similar results to the single τ_a estimation over the subscene, with lower reflectances in general and slightly larger errors and scatter. A lower number of matchups was retrieved for DSFR+GC due to the increased number of negatives retrieved with this method. The matchup results for the DSFR are shown in Figure 5 for the red and NIR I bands.

The I2gen processing provided a variable number of matchups per band, with a minimum in band M01 to a maximum in band M07. This is largely a result of the retrieval of more negatives by I2gen. Some shorter wavelength band retrievals are masked presumably because they are less than the minimum value that can be represented in the I2gen output format (i.e. $R_{rs} < -0.01$). The number of matchups varied between the different configurations, with the SWIR1 + 2 providing the most matchups ($n = 386$), nearly identical to the ACOLITE result ($n = 389$). A full series of scatter plots of the

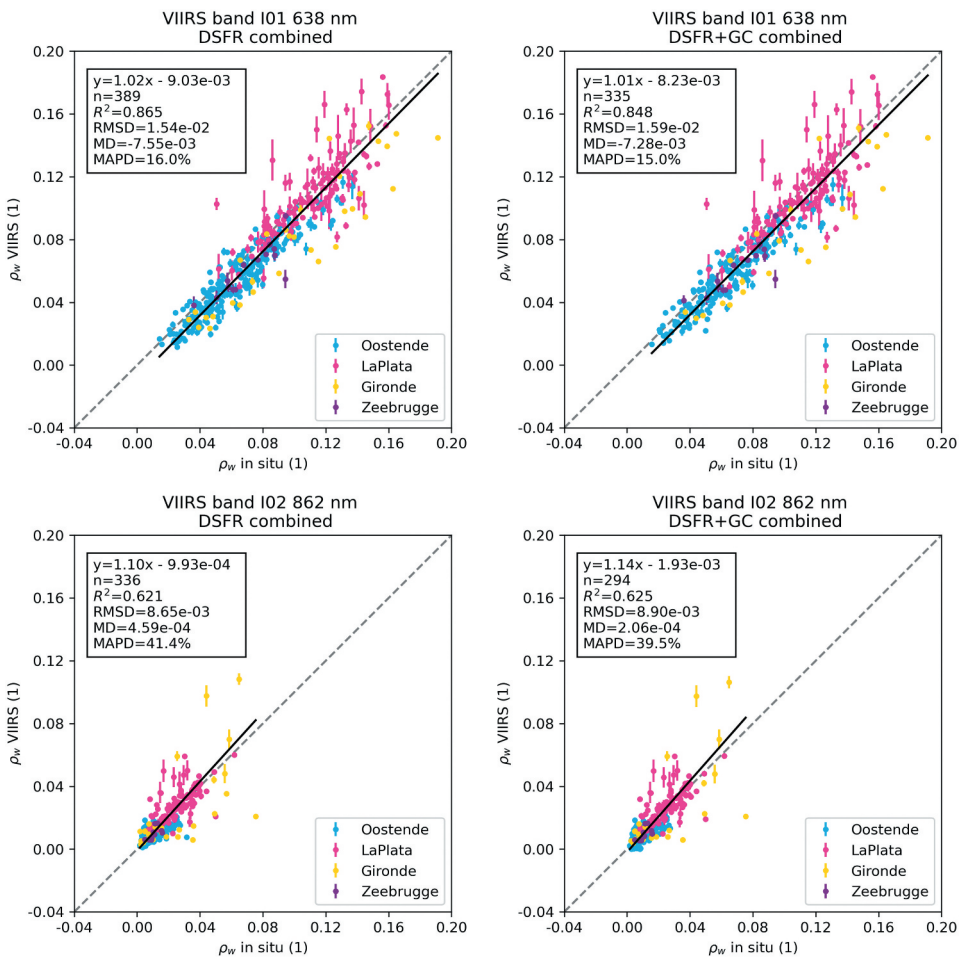


Figure 5. Same as Figure 4 but for ACOLITE/DSFR, i.e. using a per-pixel τ_a estimate.

four I2gen processing settings is provided in Supplementary Material 3. The results for the variation of I2gen where the iterative NIR correction was disabled provided even lower reflectances and larger differences with the in situ measurements. For the SWIR processing, excluding the iterative NIR also provided slightly worse results, giving lower reflectance across the spectrum. As expected, the processing with NIR bands in this variation gave almost no valid outputs for the La Plata site in the blue bands M01–M03. It did furthermore not provide NIR band reflectance (M06 and M07) for any site. The results from these processing options without iterative NIR correction are not further discussed or shown.

Spectral differences with the in situ measurements are summarized in Figures 6–8 for each processor setting across different matchup subsets for all satellite sensors combined. The dotted lines represent the total number of matchups for each individual processor. Subsets were created where both ACOLITE and I2gen provide common matchups per band, i.e. a variable number per band increasing from M01 ($n = 292$) to band M07 ($n = 371$), plotted as dashed lines, and for common matchups across all bands, i.e. where standard I2gen processing provides a full spectrum, which corresponds to its minimum valid retrievals at M01 ($n = 292$), plotted as solid lines. A breakdown per satellite sensor for these spectral errors is provided in Supplementary Material 4. Overall low differences were found for the different matchup subsets, largely due to the large amount of available matchups and the consistent processor performance. This also indicates that ACOLITE/DSF results are comparable for scenes for which I2gen processing provided data and for those for which it did not. The spectral MD (Figure 6) shows that the absolute

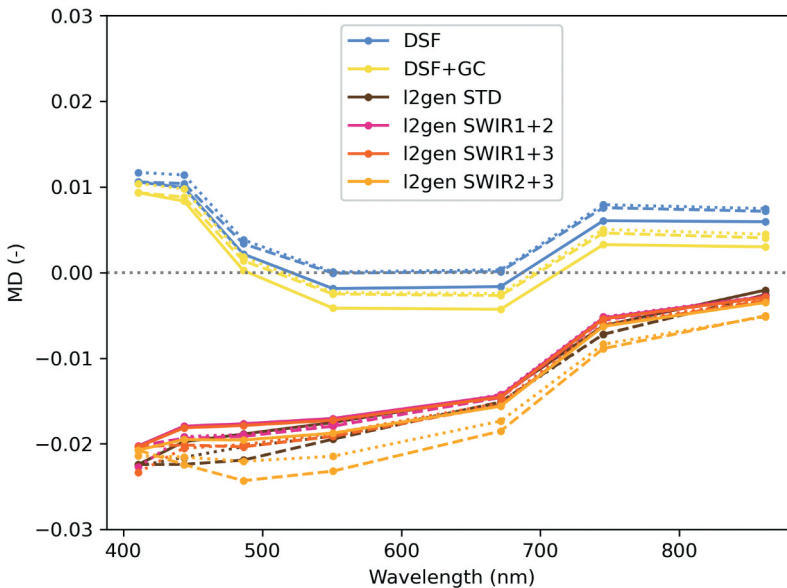


Figure 6. Mean Average Difference (MD) or the bias between in situ and satellite ρ_w measurements for the M bands as processed with ACOLITE and I2gen for all sensors combined. The solid lines represent matchups where all processors provide a full M band spectrum. The dashed lines represent the common matchups across the processors for specific band, and the dotted lines show all matchups for a given processor.

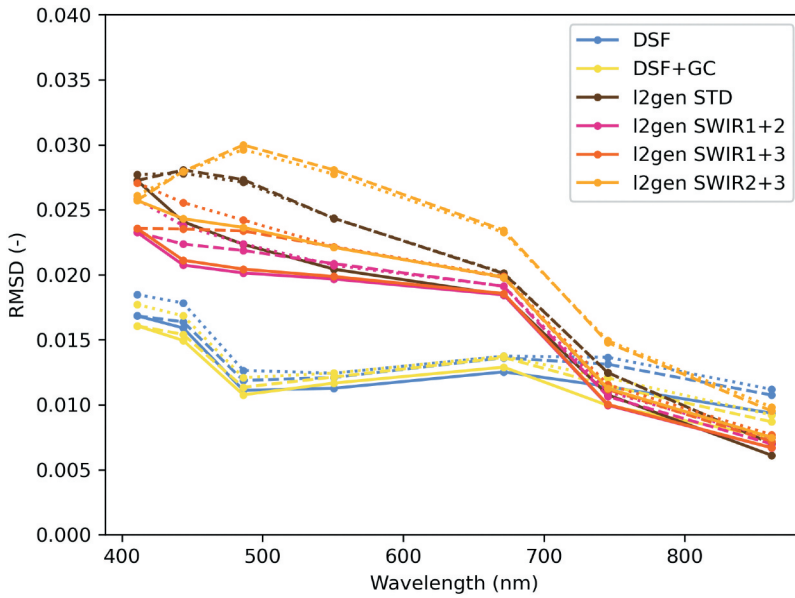


Figure 7. Same as Figure 6 but for the root mean squared difference (RMSD) representing the scatter in the matchup plots.

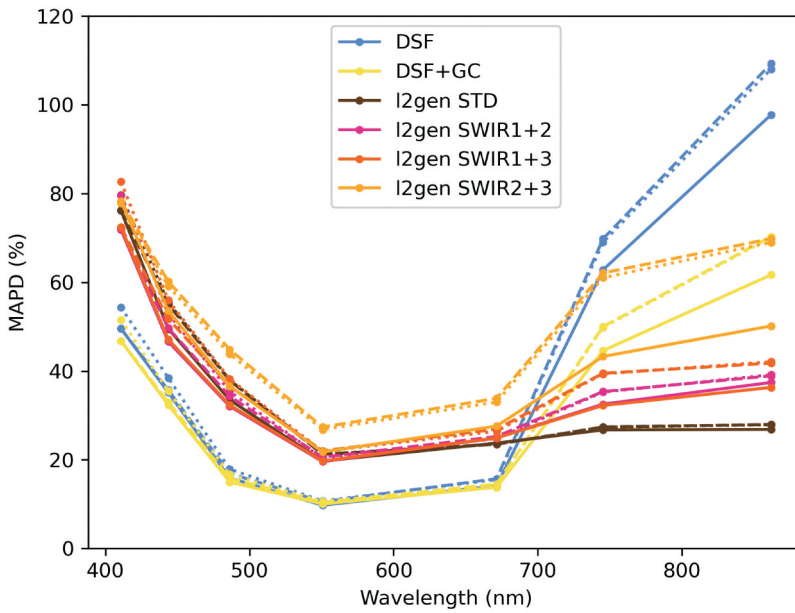


Figure 8. Same as Figure 6 but for the mean absolute percentage difference (MAPD) representing relative differences between in situ and satellite.

value of the average bias is lower in the visible bands for ACOLITE/DSF than for OCSSW/l2gen. The lowest bias is found for the blue to red bands (M03, M04 and M05) for DSF and for the NIR bands (M06 and M07) for l2gen. A larger positive bias is found for the M01 and M02 shortest blue bands in the DSF results, which is largely the result of the Suomi-NPP performance in these bands, and to a lesser extent the impact of JPSS-2 performance in M01 (see, for example, Supplementary Material 4, Fig. S12). DSF tends to overestimate the ρ_w in the shortest blue and the NIR bands, while the longer blue to red bands have a close to zero bias. The l2gen results show a negative bias across the spectrum, indicating a general overcorrection, which increases from the red to the shortest blue bands from around -0.015 to -0.020 . The spectral RMSD (Figure 7) shows a rather flat result for a DSF of around 0.01, indicating a consistent amount of scatter in the different spectral bands. An increase to almost 0.02 is found for the two shortest blue bands, which is again largely caused by Suomi-NPP (Supplementary Material 4, Fig. S13). In the NIR, l2gen gives slightly lower RMSD compared to DSF, whereas in the visible band, the RMSD is about twice that of DSF. The spectral MAPD (Figure 8) shows the increase of relative errors with decreasing water signal, with the MAPD spectrum almost looking like an inverted ρ_w spectrum. The relative differences are $< 60\%$ across the visible bands for ACOLITE/DSF, with a minimum around 10% in the green band (M04) and around 15% in the blue and red bands (M03, M05). The performance in the shortest blue bands is impacted again by the performance of Suomi-NPP, which shows 40–70% MAPD (Supplementary Material 4, Fig. S14), where JPSS-1 and JPSS-2 stay around 20–50%. The relative differences increase towards the NIR, reaching 100% in M07. The glint correction has the largest impact on the NIR reflectance matchups reducing relative differences from 60–100% to 40–60%. For l2gen, the visible band relative differences follow the same trend but are higher compared to DSF, i.e. $< 80\%$ in the visible, reaching 20–30% in the best performing bands. The NIR performance shows flatter and lower relative differences (20–40%) in general compared to DSF, especially for the standard processing and the SWIR-based processing using the SWIR1 band at around $1.2 \mu\text{m}$ (M08).

4. Discussion

4.1. DSF validation results

Our results show that ACOLITE/DSF can accurately perform the atmospheric correction for both I and M band sets on VIIRS. While the bands used for estimating the τ_a and aerosol model are determined automatically, the DSF relies heavily on the SWIR bands for the atmospheric correction over the turbid waters of the study sites. The red (I01) and NIR (I02) I band reflectances reach relative differences with in situ measurements of on average 13% for I01 and 96% (without glint correction) to 60% (with glint correction) for I02. These performances are comparable to the spectrally close coarser resolution M05 and M07 bands. ACOLITE/DSF can also retrieve surface level reflectance (ρ_s) for the SWIR (I03) I band, a channel that contains no water leaving signal ρ_w , but that can be used to determine sun glint on the air–water interface or for the retrieval of floating/above water objects. The use of the DSF with a SWIR-based per-pixel glint correction applied after the atmospheric correction provided slight improvements especially in the NIR channels (I02, M05 and M07). The impact on the matchup statistics of the glint correction is rather small

as most heavily glinted scenes are excluded by the default quality control in ACOLITE. Although the matchup locations are close to land, we find no clear impacts of land and vegetation adjacency effects (AE), largely due to relative insensitivity of the DSF to these types of AE, especially in the visible bands where the land and vegetation signal is rather low. Due to the large red-edge signal of vegetation, however, the NIR band results may have a larger impact from AE, which will still be included in the reflectance output by DSF. In other conditions, e.g. near very bright and spectrally flat ice or snow surfaces, the AE may prove to be more problematic for the DSF, as they are for many other atmospheric correction approaches. In our dataset, no such conditions are present. The explicit correction of AE is not attempted in any currently operational processor and is a topic of active research. The per-pixel application of the DSF, i.e. DSFR, showed a good performance overall, with similar average statistics compared to the application of the DSF with fixed aerosol over a 36×36 km subscene. The DSFR I01 band results showed a slight decrease in performance compared to the DSF, e.g. the average relative differences increased from 13 to 16%, while the NIR I02 band performance improved with the relative differences reduced to around 44%. This indicates that a residual signal is present in the DSF NIR outputs, which can be improved by treating it as an aerosol signal in the DSFR. Although slightly more noisy outputs were found for the DSFR, the noise level and calibration of the NIR and SWIR bands seem to be acceptable for per-pixel processing. For larger regions of interest, regions with strong spatial variability in aerosol concentration, or for full scene processing, the use of a single τ_a is not likely to be appropriate, and the DSFR may provide better results compared to the DSF. For small regions of interest, e.g. processing at the level of an estuary or inland water body, the use of DSF rather than DSFR may provide smoother output products, with lower sensitivity of the aerosol correction to NIR/SWIR land and vegetation adjacency effects.

4.2. SeaDAS/I2gen results

For the M bands, ACOLITE/DSF results more closely corresponded to the turbid water measurements in this study compared to OCSSW/I2gen, especially for the visible bands where I2gen showed signs of overcorrection for aerosols. An analysis of the I2gen aerosol retrieval parameters, i.e. τ_a in band M07 around 862 nm, and the Ångström exponent (α), shows that this overcorrection in the visible bands is correlated with α . Scatter plots of ρ_w difference (satellite – in situ) in band M01 (around 412 nm) as a function of the retrieved τ_a and α for I2gen are provided in Supplementary Material 5 (Figs. S15 and S16). These show that the overcorrection of visible band ρ_w can be linked to α estimation, with the largest underestimation of ρ_w ($\Delta\rho_w$ –0.05 to –0.07) occurring for the highest values of α (1.4 to 1.8). Only a slight trend between $\Delta\rho_w$ and τ_a is observed, at least for the SWIR based models. The rather good fit of I2gen results to the in situ measurements in the NIR also indicates that the τ_a is well estimated. A larger range of α is found for I2gen STD, where the water reflectance contaminates the aerosol retrieval. Especially for LaPlata and I2gen STD, there is a strong correlation between $\Delta\rho_w$ and the τ_a retrievals, and the α estimate tends towards the maximum available value in the used aerosol model set. The aerosol parameter maps derived from the SWIR based methods did not show clear patterns of turbid water contamination, while the STD method did show impacts of non-zero NIR water reflectance (an example is shown in Supplementary Material 5, Figs. S17, S18, and

S19). As the τ_a and NIR ρ_w retrievals seem to be rather accurate, the model selection procedure may need to be improved, and perhaps the correct model cannot be estimated from the wide range of available models using only two NIR or SWIR observations. The main issue with I2gen VIIRS processing for turbid waters at present seems to be the tendency to select aerosol models with a high Ångström exponent, i.e. with a large fine mode fraction.

4.3. Mission consistency

Mostly the same average performance was found across the three satellite missions. Even with a lower total number of matchups ($n = 22$) due to the recency of the mission, JPSS-2 performance compared well to the across mission average and the other missions separately, even though the matchup data cover only a few months in northern hemisphere winter and spring. Higher positive biases were found for the DSF processing of Suomi-NPP blue bands (M01 and M02) compared to the processing of JPSS-1 and JPSS-2. These bands also showed a correspondingly higher relative difference and a bit more scatter compared to other bands. These differences were not present in the I2gen outputs, where results were more closely aligned for M01 and M02 across the sensors, albeit with a larger negative bias, presumably due to the application of large top-of-atmosphere vicarious calibration gains to the Suomi-NPP blue bands (Table 3). The application of these gains in the ACOLITE/DSF processing shows an improvement in the matchup analysis for the M bands on Suomi-NPP, especially in the blue bands, but does not improve results for JPSS-1 and JPSS-2 (not shown separately). This is largely an effect of the smaller than unity gains correcting some of the ACOLITE/DSF positive bias for Suomi-NPP, while the larger than unity gains for JPSS-1 and JPSS-2 further increase the ACOLITE/DSF positive bias. The Suomi-NPP spectra appear smoother in the blue–green spectral region after the application of these gains, removing the bump around M01–M02–M03, which is visible for example in the ACOLITE/DSF results in the top right plot of Figure 3 and in the spectral error plots in Supplementary Material 4. Of course, these gains are specific to the OCSSW/I2gen processing system and are not recommended for general use with ACOLITE.

4.4. Regional differences

Across the different validation sites, lower scatter was observed for the Belgian sites (O1BE and M1BE) compared to the Argentinean (LPAR) and French (MAFR) sites (Figures 4 and 5 and Supplementary Materials 2 and 3). In particular, more scatter was found in the red and NIR bands for LPAR and MAFR, where much higher reflectances were observed compared to the Belgian sites. The visible bands

Table 3. Vicarious calibration gains of the first six M bands of the three VIIRS instruments as implemented in OCSSW/I2gen processing version 2023.2. These are determined over clear oceanic waters using the standard processing; NIR band gains are set to 1.

| Satellite | M01 | M02 | M03 | M04 | M05 | M06 |
|-----------|---------|----------|----------|----------|----------|----------|
| Suomi-NPP | 0.96571 | 0.95267 | 0.98339 | 0.98540 | 0.99177 | 0.97731 |
| JPSS-1 | 1.00907 | 1.008178 | 1.019374 | 1.014986 | 1.003158 | 0.993086 |
| JPSS-2 | 1.02100 | 1.02482 | 1.01097 | 0.99667 | 1.01617 | 1.00219 |

compared similarly across all sites, and more limited reflectance ranges around the matchup location were found, i.e. the vertical error bars in the scatter plots are smaller in the visible than in the NIR bands. This more limited reflectance range for the visible bands around the matchup location is consistent with the saturation of reflectance in turbid and extremely turbid waters (Doxaran et al. 2002; Luo et al. 2018). Under saturated conditions, a band will no longer be sensitive to changes in particulate concentration, and close to these conditions, differences in particulate concentration will lead to low (or no) differences in reflectance. Saturated bands can thus provide good correspondence for a larger range of turbidity, as changes in the concentration of suspended particles caused by spatial and temporal variability or mismatch may be masked by the saturated reflectance. The wavelength under which saturation reflectance occurs depends on the particulate type and concentration, with blue bands showing saturation effects first and NIR bands showing them last. For the red and NIR bands at LPAR, a good agreement was found, however, with a large standard deviation in the 3×3 pixel box. This indicates that spatial variability occurs at the scale of the VIIRS pixel near the reference pixel location, which is hidden by the reflectance saturation in the blue and green bands that have much lower standard deviations. Some of this spatial variability can be perhaps seen in the Sentinel-2 image in Figure 2, but it remains largely invisible due to the saturated reflectance of the water. High resolution imagery around the site (not shown separately) indicates that there is largely a gradual trend of changing reflectance from the coast to the middle of the estuary, especially at red wavelengths, which was also observed, for example, by A. I. Dogliotti et al. (2015). This trend is discretised by the different VIIRS pixels and shows up as pixel-to-pixel differences and hence as increased standard deviation in the matchup box. For the red and NIR bands at the MAFR site, larger, both positive and negative, differences between in situ and satellite were found. The effects of reflectance saturation in the shorter wavelength bands also here lead to a better performance of those bands in the matchup results, i.e. the shorter wavelength bands are not significantly affected by changes in particulate concentration observed at the site. The low standard deviation at the reference location shows that it is rather homogeneous at the VIIRS pixel size, and the difference in red and NIR band reflectance is hence likely the result of spatial variability between the near-shore site and the reference pixel further towards the centre of the estuary. Large variability occurs throughout the estuary, with turbidity and hence reflectance usually highest near the shores and dropping off towards the centre (e.g. Novoa et al. 2017; Luo, Doxaran, and Vanhellemont 2020)). In contrast to the other sites that are installed 0.5 km to 5 km offshore on slender platforms, the MAFR instrument is installed on a rather large near-shore mooring pontoon, with its reference matchup location several hundred metres away. The currents around the underwater structures of the pontoon may create very dynamic and small scale turbidity patterns near the measurement location. The challenging location of MAFR may perhaps limit its use to validation of higher spatial resolution sensors such as the decametre scale imagers on board Landsat and Sentinel-2. Removing the MAFR ($n=32$) data from the total number of matchups ($n=389$) in the present study however only has a minor impact on the average matchup statistics (not shown separately).

4.5. Applications

In this section, some example applications using the VIIRS I band data as processed by ACOLITE/DSF are presented. These algorithms are available from the literature but are here adapted and integrated in ACOLITE for using the VIIRS I (or M) bands. These products can be directly output from the open source processor, serve as demonstration products of the new ACOLITE capability, and could inspire potential users. Results presented here were reprojected to a common 375×375 m UTM grid for both I and M bands.

The red and NIR M and I band data can be used to compute a high resolution switching turbidity product, e.g. using the algorithm and calibration of Nechad, Ruddick, and Neukermans (2009) with the blending method of A. I. Dogliotti et al. (2015) or Novoa et al. (2017). An example of such turbidity products generated from 750 m M and 375 m I band data is shown in Figure 9. The I band product shows a much sharper image, with clearer delineation of turbidity features. The turbidity in this area is largely determined by resuspension and bathymetry, and the location of shallower sandbank areas for example can be much more clearly seen on the I band product. In this particular example, the I band product shows a higher data range (3.2–40.8 FNU) compared to the M band product (4.5–38.4 FNU), and its spatial resolution may be better suited to resolve peak turbidity values (e.g. Ody et al. (2016); Dorji, Fearn, and Schumann (2017)). Near-shore mixed pixels were masked using the observed differences between I03 and M10 SWIR bands at $1.6 \mu\text{m}$, but this criterion could be relaxed if only the I band data is of interest, with a masking based on I03 alone.

The ρ_s data from the first three I bands can also be used to compute a floating algal index (FAI, Hu (2009)) at 375 m resolution. A FAI map produced from an image acquired during the early 2016 massive floating plant event in the La Plata estuary, as described in A. Dogliotti et al. (2018), is shown in Figure 10 using an M (750 m) and I (375 m) band combination. This figure demonstrates the additional resolving power of the higher resolution product and its potential in improving detection and monitoring of floating algal matter. To determine estuarine pixels, the land area was masked using the Copernicus 30 m global DEM (DOI: [10.5270/ESA-c5d3d65](https://doi.org/10.5270/ESA-c5d3d65)) reprojected to the same UTM

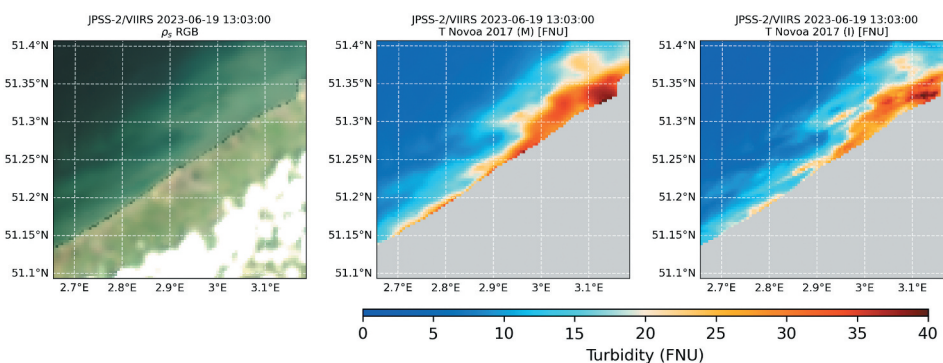


Figure 9. JPSS-2/VIIRS scene acquired 2023-06-19 (13:03 UTC) over O1BE, as processed with ACOLITE/DSF+GC showing ρ_s RGB composite (left) and the red and NIR blended turbidity retrievals according to algorithms of Nechad, Ruddick, and Neukermans (2009); Novoa et al. (2017) using the M bands at 750 m (middle) and the I bands at 375 m (right).

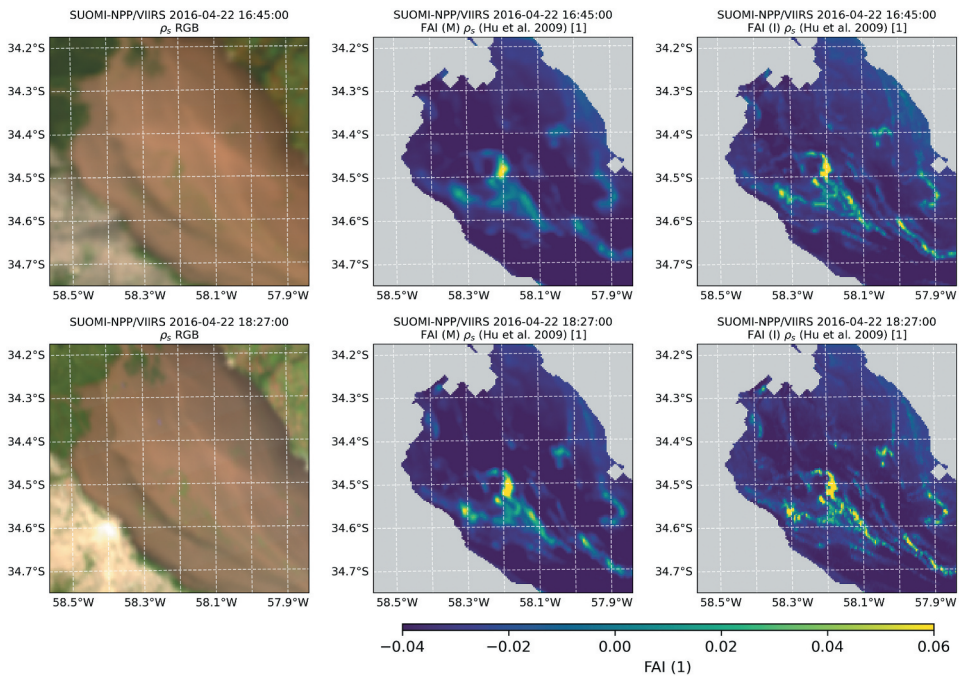


Figure 10. Example of two Suomi-NPP/VIIRS scenes of the La Plata estuary near Buenos Aires (upstream of the LPAR site) taken 2016-04-22 at 16:45 UTC (top) and 18:27 UTC (bottom) during a massive floating plants event (A. Dogliotti et al. 2018). Shown are the ρ_s RGB composite (left) and the retrieval of a 750 m M band (middle) and 375 m I band (right) floating algal index according to Hu (2009).

grid. Pixels above the sea level were masked and buffered using 5 binary dilation operations in order to exclude land, near-shore and mixed land-water pixels to which the FAI is sensitive. The surface areas of estuarine pixels with $\text{FAI} > -0.004$ (Hu et al. 2010) were 70 km² and 117 km² for the 16:45 UTC image, and 111 km² and 127 km² for the 18:27 UTC image, for the M and I band FAI, respectively. A larger difference in the areal estimates was found for the M band product, presumably due to the larger pixel size, especially at the edge of swath viewing conditions (θ_v was 65.5° at 16:45 UTC and 54.3 at 18:27 UTC). Due to the movement of the floating algal patches between both overpasses, their horizontal transport can be estimated. In this example, the patches moved about 3 km downstream between the Suomi and NPP overpasses spaced 102 minutes apart, indicating a surface current of about 0.5 m/s. The use of the I band product simplified the identification of the patches and their edges on the subsequent images.

It is possible to relax the masking thresholds so that ACOLITE can provide outputs for specific use cases in more severely glinted conditions; an example is given in Figure 11. This scene has large ρ_t SWIR, with M10 for most water pixels being greater than the masking default (0.0215) and reaching up to 0.08. By increasing the ACOLITE masking and glint thresholds to 0.08, water reflectance can still be retrieved with the glint signal present (DSF) or largely removed (DSF+GC). Some residual glint patterns remain in the DSF+GC data, especially in the NIR I02 band, but the water turbidity features, especially in the red I01 band and other visible bands, are more clearly resolved. As a result of the glint

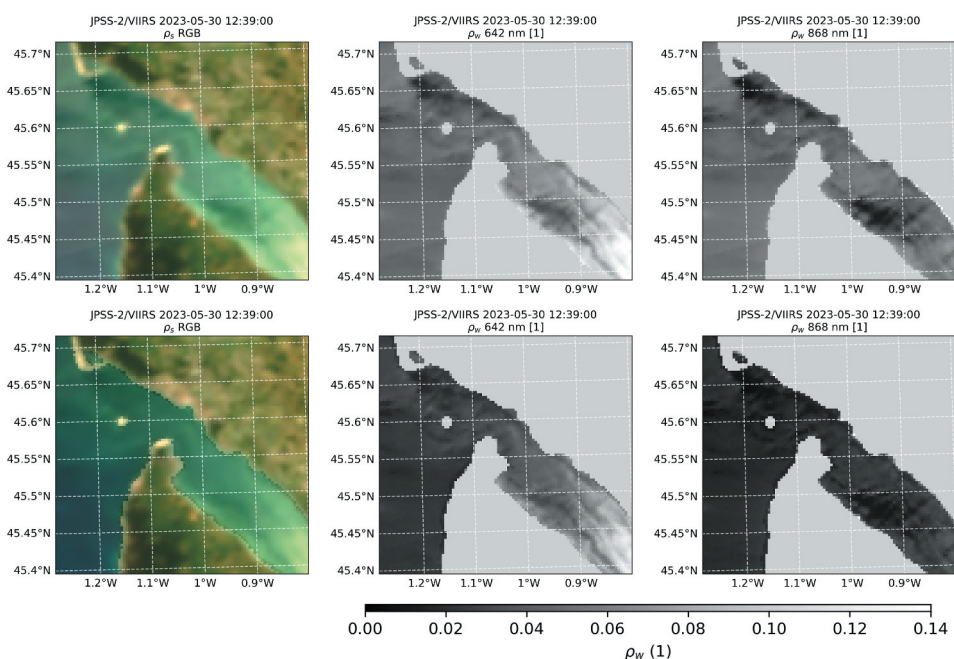


Figure 11. Example of a JPSS-2/VIIRS scene with severe glint acquired 2023-05-30 at 12:39 UTC over the MAFR site. The top row shows the ρ_s RGB composite, I01 red and I02 NIR band ρ_w retrieval without glint correction, and the bottom row shows the same with glint correction. In this example, the thresholds (on ρ_s in I03) for masking and glint correction were increased from the defaults to 0.08. The variability mask using I03 and M10 was disabled.

viewing geometry, the scan edges can be more clearly seen in the DSF processed data, while they are largely removed after DSF+GC processing. This processing option gives larger uncertainties on the resulting ρ_w data and is hence better suited for targets with high turbidity and associated high ρ_w .

As shown above in the floating algal example, multiple VIIRS overpasses, even from the same sensor, can be available for a given day. By combining data from the three operational wide-swath VIIRS sensors, it may be possible to observe temporal variability between their different overpass times. An example for the O1BE site on 16 May 2023 is provided in Figure 12, where five VIIRS images were available in a two-hour period between 11:39 UTC and 13:45 UTC. The data in this time series plot have their quality masking relaxed compared to the matchup analysis, and glint correction was applied (see, for example, the steps taken in the previous paragraph). Mainly, the I to M band sub-pixel variability test was masking large amounts of pixels, possibly as a result of high spatial variability and more pixel mixing at high viewing zenith angles. Overall, these show good performance for two I band matchups, one from Suomi-NPP at 12:33 UTC and one JPSS-1 at 13:21 UTC. The larger difference with the in situ measurement for the other matchups (of around 0.01–0.02) could be caused by the presence of spatial variability between the measurement and reference locations (see also, for example, the top left panel of Figure 2) that could be different at different stages of the tide, e.g. as a result of tidal monopile wakes or the port outflow. The higher PANTHYR reflectance before the VIIRS overpasses,

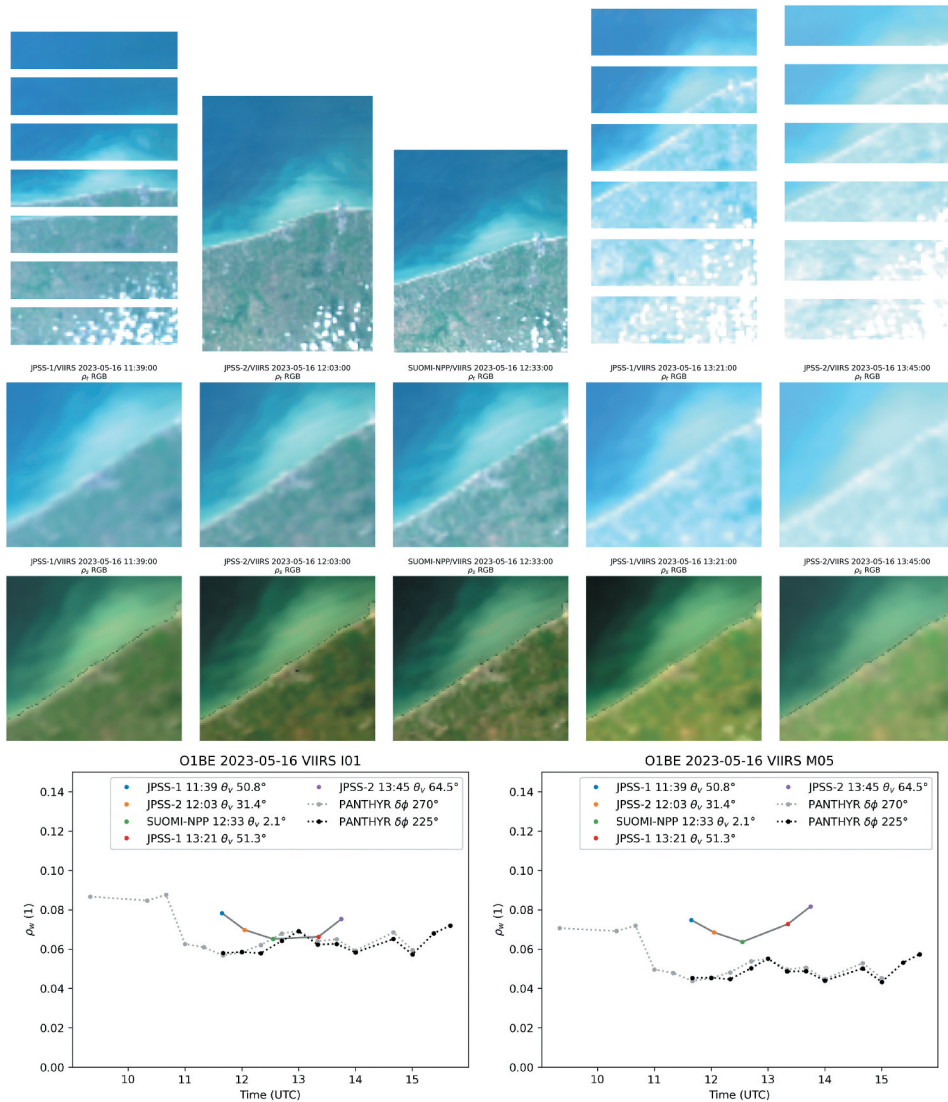


Figure 12. Multiple observations by VIIRS for the O1BE site on 2023-05-16 as processed using ACOLITE/DSF+GC. The top two rows show the unprojected and projected ρ_r , and the third row shows the ρ_s RGB composite. Reflectance was scaled from 0 to 0.15 to fit the 8 bit channels in the RGB. The lower plots show the temporal variability of the red band ρ_w as observed by PANTHYR (at $\delta\phi$ 225° and 270°) and the operational VIIRS constellation for I01 at around 640° nm (left) and M05 at around 670° nm (right). The legend indicates the VIIRS view zenith angle (θ_v). Local solar noon is around 11:45 UTC, and θ_s varied between 32.1° at 11:39 UTC and 39.7° at 13:45 UTC. Data were acquired during ebb, high tide was around 10 UTC, and low tide was around 16 UTC. Latitude and longitude annotations are suppressed for legibility, and can in fact not be displayed for unprojected data. The extents are the same as in Figures 3 and 9.

i.e. between 9 and 11 UTC, is indicative of the flood tide platform wake being observed by the instrument. A SuperDove image taken on 16 May 2023 at 9:54 UTC, i.e. before the VIIRS overpasses and during the flood tide, showed considerable spatial variability, including around the RT1 measurement tower, and at the reference location. In this image, the reflectance in the red and red-edge bands was around 0.03 lower at the measurement location compared to the reference location 600 m away, i.e. of the same magnitude as the VIIRS differences observed here. The SuperDove image and a transect across the near-shore area are provided in Supplementary Material 6 (Fig. S20). Compared to the I band, the M band result shows a larger difference with the in situ measurement. This difference between the red I and M bands is not present in the matchup analysis presented earlier and is presumably also the result of small scale variability around the validation and reference sites. The higher observation angle data at the beginning and end of the VIIRS time series show larger difference with the in situ measurements, possibly as a result of directional effects not accounted for. These data may also be impacted by longer atmospheric path lengths and increased pixel size for the observations with higher viewing zenith angle (θ_v). The ρ_s RGB appears more blurry, and seems to have a blue haze, indicating issues with pixel size and residual atmospheric or air–water interface reflectance. Note also the brighter ρ_t RGB composites for these images as a result of the longer atmospheric path length. Overall, these results show the usual difficulties in matching up moderate resolution satellite data with in situ measurements in waters with high temporal and spatial variability and processing of imagery with long atmospheric path lengths. Nonetheless, depending on the application, useful information could be retrieved from multiple VIIRS observations during the day.

5. Conclusions

In the present paper, the processing of VIIRS I and M bands with ACOLITE/DSF was presented. The results compared well to several hundreds of matchups across three satellite sensors (on board Suomi-NPP, JPSS-1 and JPSS-2) and four turbid water sites equipped with autonomous hyperspectral radiometers. The best performing bands were those with the highest water signal, i.e. bands between 490 and 670 nm. Mean absolute differences in those bands were close to zero, with mean absolute percentage differences around 10–15%. Due to the high turbidity, appreciable reflectance in the NIR channels was observed, where ACOLITE/DSF provided reasonable estimates, in general with relative differences $< 50\%$. The performance of the two red (I01) and NIR (I02) I channels was found to be on par with that of the corresponding M channels (M05 and M07), indicating that they can be used for turbidity mapping in turbid waters. The optional glint correction provided a small benefit across the spectrum, but it should be noted that the most severe glint observations are filtered out by the thresholds in the masking procedure.

In general, the same patterns were observed across the different satellite platforms. JPSS-1 provided the best performance overall, with Suomi-NPP giving slightly larger differences, especially in the two shortest wavelength bands (M01 and M02 at around 412 and 443 nm), likely as a result of top-of-atmosphere calibration. JPSS-2 gave very similar performance to JPSS-1, with slightly higher differences in band M01. A lower number of JPSS-2 data were available from its commissioning phase, mostly from the northern hemisphere winter and spring, i.e. with lower sun elevations. Overall, the VIIRS

data from all three platforms can be used in combination for the types of waters investigated here, especially in the range 490–670 nm. The potential use of top-of-atmosphere system vicarious calibration gains to improve the ACOLITE processing may need investigation.

OCSSW/l2gen processing of the VIIRS M bands was also tested for a series of settings. Results from l2gen showed higher scatter, as well as larger absolute and relative differences compared to ACOLITE/DSF, except in the NIR bands, where l2gen reflectance is more constrained. For all sites, l2gen using the SWIR bands gave improved performance over the standard configuration, with on average SWIR1 + 3 providing the best results. The alternative and simpler two band atmospheric correction settings without NIR iteration did not provide satisfactory results. The results presented here indicate that the overcorrection by l2gen in the visible bands is largely due to the selection of aerosol models with a large Ångström exponent, i.e. those with a large fine mode fraction. The SWIR-based l2gen processing did not show correlation of the aerosol parameters to in situ-measured water reflectance, indicating that the water signal did not affect the aerosol model selection. These findings may illustrate the difficulty of selecting an appropriate aerosol model from a large selection using only two NIR or SWIR bands.

The present paper demonstrates once more the power of a network of hyperspectral in situ instruments (K. Ruddick et al. 2024) for the validation of optical VSWIR satellite missions, with varying band sets and widths. Data from the PANTHYR and HYPSTAR®-SR instruments can be used to validate any satellite band within 400–900 nm, and, in particular for land deployments, with the HYPSTAR®-XR (eXtended Range) up to 1700 nm. For the present study, matchups were already available within the first few months of the JPSS-2 satellite mission, which provide timely information on the instrument performance. For the different validation sites, a better understanding of the behaviour of the reference and measurement locations may be needed, and perhaps sensor specific matchup suitability and reference locations are needed. Determining these may require the combination of high frequency metre scale imagery, in-water sensor deployments, and hydrodynamical modelling efforts. It should be noted that most in situ deployment locations are opportunistic, as well as the use of their data in many cases. An in depth characterization of the different sites in the network, e.g. also with regards to optical and physical impacts of the deployment platform, will aid the understanding of the performance and the uptake of their measurements.

Examples of VIIRS high resolution turbidity and floating algal products were presented, as well as the potential for tracking temporal variability or horizontal transport by using multiple VIIRS observation throughout the day. ACOLITE is currently the only freely available and open source processor with the capability of processing both VIIRS I and M bands at native resolution. The availability of this processor could enable more users to access the higher resolution I band data for improved mapping of turbid waters or floating materials.

Acknowledgments

NASA and NOAA are thanked for the acquisition and free distribution of VIIRS imagery, and the NASA/OBPG is thanked for the distribution of the OCSSW package. ESA/Copernicus is thanked for the acquisition and free distribution of Sentinel-2 data. Planet is thanked for research access to

SuperDove imagery. The Flanders Marine Institute (VLIZ) and POM West-Vlaanderen are thanked for access to the RT1 Blue Accelerator Platform (Oostende, Belgium) and installation support. The Escuela Naval Militar (EsNM) and Servicio de Hidrografía Naval (SHN) are thanked for permission and access to the LPAR platform and installation support. L. Rubinstein, E. Piegari, P. Perna, and U. Hereñú are thanked for the technical support. Dmitry Van der Zande is thanked for advising and helping in deploying the system, and Anabel Gammaru is thanked for managing the M1BE site. The Maritieme Dienstverlening en Kust Vlaanderen and their contractors are gratefully acknowledged for logistical support and access to the MOW1 platform near Zeebrugge for the M1BE deployment. This study was funded partially by the European Space Agency under the HYPERNET-POP contract and also used data generated by the H2020/HYPERNETS project of the European Union.

Disclosure statement

No potential conflict of interest was reported by the author(s).

Funding

The work was supported by the European Commission [H2020/HYPERNETS]; European Space Agency [HYPERNET-POP].

ORCID

Quinten Vanhellemont  <http://orcid.org/0000-0001-9195-6347>

Data availability statement

The VIIRS data that support the findings of this study are available from NASA Ocean Color (<https://oceancolor.gsfc.nasa.gov/>, accessed 18 March 2024) and NASA EarthData (<https://www.earthdata.nasa.gov/>, accessed 18 March 2024) and were processed using open source software OCSSW (<https://oceandata.sci.gsfc.nasa.gov/ocssw/>, accessed 18 March 2024) and ACOLITE (<https://github.com/acolite/acolite>, accessed 18 March 2024). In situ datasets from PANTHYR and HYPSTAR® data were obtained from the following public data releases: O1BE Vansteenwegen and Vanhellemont (2023), LPAR (A. I. Dogliotti et al. 2023), MAFR (Doxaran and Corizzi (2023)), and M1BE (Goyens and Gammaru 2023). Additional PANTHYR data from the current deployment at O1BE were also used and can be made available at request. These data will be made available publicly after the completion of the deployment.

CRedit author statement

Quinten Vanhellemont: Conceptualization, Methodology, Software, Formal analysis, Data curation, Writing- Original draft preparation, Visualization. **Ana Dogliotti:** Investigation, Writing – Reviewing and Editing. **David Doxaran:** Investigation. **Clémence Goyens:** Investigation, Writing – Reviewing and Editing. **Kevin Ruddick:** Project administration, Funding acquisition, Writing – Reviewing and Editing. **Dieter Vansteenwegen:** Investigation.

References

Ahmad, Z., B. A. Franz, C. R. McClain, E. J. Kwiatkowska, J. Werdell, E. P. Shettle, and B. N. Holben. 2010. "New Aerosol Models for the Retrieval of Aerosol Optical Thickness and Normalized

- Water-Leaving Radiances from the SeaWiFS and MODIS Sensors Over Coastal Regions and Open Oceans." *Applied Optics* 49 (29): 5545–5560. <https://doi.org/10.1364/AO.49.005545>.
- Bailey, S. W., B. A. Franz, and P. Jeremy Werdell. 2010. "Estimation of Near-Infrared Water-Leaving Reflectance for Satellite Ocean Color Data Processing." *Optics Express* 18 (7): 7521–7527. <https://doi.org/10.1364/OE.18.007521>.
- Balasubramanian, S. V., N. Pahlevan, B. Smith, C. Binding, J. Schalles, H. Loisel, D. Gurlin, et al. 2020. "Robust Algorithm for Estimating Total Suspended Solids (TSS) in Inland and Nearshore Coastal Waters." *Remote Sensing of Environment* 246:111768. <https://doi.org/10.1016/j.rse.2020.111768>.
- Barnes, B. B., J. P. Cannizzaro, D. C. English, and C. Hu. 2019. "Validation of VIIRS and MODIS Reflectance Data in Coastal and Oceanic Waters: An Assessment of Methods." *Remote Sensing of Environment* 220:110–123. <https://doi.org/10.1016/j.rse.2018.10.034>.
- Chen, Z., C. Hu, and F. Muller-Karger. 2007. "Monitoring Turbidity in Tampa Bay Using MODIS/Aqua 250-M Imagery." *Remote Sensing of Environment* 109 (2): 207–220. <https://doi.org/10.1016/j.rse.2006.12.019>.
- De Vis, P., C. Goyens, S. Hunt, Q. Vanhellemont, K. Ruddick, and A. Bialek. 2024. "Generating Hyperspectral Reference Measurements for Surface Reflectance from the LANDHYPERNET and WATERHYPERNET Networks." *Frontiers in Remote Sensing* 5:1347230. <https://doi.org/10.3389/frsen.2024.1347230>.
- Dogliotti, A., J. Gossn, Q. Vanhellemont, and K. Ruddick. 2018. "Detecting and Quantifying a Massive Invasion of Floating Aquatic Plants in the Ro de la Plata Turbid Waters Using High Spatial Resolution Ocean Color Imagery." *Remote Sensing* 10 (7): 1140. <https://doi.org/10.3390/rs10071140>.
- Dogliotti, A. I., J. Ignacio Gossn, Q. Vanhellemont, and K. G. Ruddick. 2015. "Evaluation of Two Sites for Ocean Color Validation in the Turbid Waters of the Rio de la Plata (Argentina)." *Proceedings of the Sentinel-3 for Science Workshop held in Venice-Lido, Italy, 2-5 June 2015, ESA Special Publication SP, Palazzo del Casino, Venice Lido, Italy, Vol. 734*.
- Dogliotti, A. I., E. Piegari, L. Rubinstein, and P. Perna. 2023. "Initial Sample of HYPERNETS Hyperspectral Water Reflectance Measurements for Satellite Validation from the LPAR Site (Argentina)." <https://doi.org/10.5281/zenodo.8057728>.
- Dorji, P., P. Fearn, and G. J.-P. Schumann. 2017. "Impact of the Spatial Resolution of Satellite Remote Sensing Sensors in the Quantification of Total Suspended Sediment Concentration: A Case Study in Turbid Waters of Northern Western Australia." *PLOS ONE* 12 (4): e0175042. <https://doi.org/10.1371/journal.pone.0175042>.
- Doxaran, D., and A. Corizzi. 2023. "Variations of Suspended Particulate Matter Concentrations of the Mackenzie River Plume (Beaufort Sea, Arctic Ocean) Over the Last Two Decades." *Marine Pollution Bulletin* 196:115619. <https://doi.org/10.5281/zenodo.8057789>.
- Doxaran, D., J.-M. Froidefond, P. Castaing, and M. Babin. 2009. "Dynamics of the Turbidity Maximum Zone in a Macrotidal Estuary (The Gironde, France): Observations from Field and MODIS Satellite Data." *Estuarine, Coastal and Shelf Science* 81 (3): 321–332. <https://doi.org/10.1016/j.ecss.2008.11.013>.
- Doxaran, D., J.-M. Froidefond, S. Lavender, and P. Castaing. 2002. "Spectral Signature of Highly Turbid Waters: Application with SPOT Data to Quantify Suspended Particulate Matter Concentrations." *Remote Sensing of Environment* 81 (1): 149–161. [https://doi.org/10.1016/S0034-4257\(01\)00341-8](https://doi.org/10.1016/S0034-4257(01)00341-8).
- Franz, B. A., P. Jeremy Werdell, G. Meister, E. J. Kwiatkowska, S. W. Bailey, Z. Ahmad, and C. R. McClain. 2006. "MODIS Land Bands for Ocean Remote Sensing Applications." *Proceedings Ocean Optics XVIII* 9–13, Vol. 10, Montreal, Canada.
- Gordon, H. R., and M. Wang. 1994. "Retrieval of Water-Leaving Radiance and Aerosol Optical Thickness Over the Oceans with SeaWiFS: A Preliminary Algorithm." *Applied Optics* 33 (3): 443–452. <https://doi.org/10.1364/AO.33.000443>.
- Goyens, C., and A. Gammaru. 2023. "Improving the Standard Protocol for Above-Water Reflectance Measurements: 1. Estimating Effective Wind Speed from Angular Variation of Sunlight." *Applied Optics* 62 (10): 2442–2455. <https://doi.org/10.5281/zenodo.8059881>.

- Harmel, T., M. Chami, T. Tormos, N. Reynaud, and P.-A. Danis. 2018. "Sunlight Correction of the Multi-Spectral Instrument (MSI)-SENTINEL-2 Imagery Over Inland and Sea Waters from SWIR Bands." *Remote Sensing of Environment* 204:308–321. <https://doi.org/10.1016/j.rse.2017.10.022>.
- Hlaing, S., T. Harmel, A. Gilerson, R. Foster, A. Weidemann, R. Arnone, M. Wang, and S. Ahmed. 2013. "Evaluation of the VIIRS Ocean Color Monitoring Performance in Coastal Regions." *Remote Sensing of Environment* 139:398–414. <https://doi.org/10.1016/j.rse.2013.08.013>.
- Hu, C. 2009. "A Novel Ocean Color Index to Detect Floating Algae in the Global Oceans." *Remote Sensing of Environment* 113 (10): 2118–2129. <https://doi.org/10.1016/j.rse.2009.05.012>.
- Hu, C., Z. Lee, R. Ma, K. Yu, D. Li, and S. Shang. 2010. "Moderate Resolution Imaging Spectroradiometer (MODIS) Observations of Cyanobacteria Blooms in Taihu Lake, China." *Journal of Geophysical Research Oceans* 115 (C4): 115 (C4). <https://doi.org/10.1029/2009JC005511>.
- Kotchenova, S. Y., E. F. Vermote, R. Matarrese, and F. J. Klemm Jr. 2006. "Validation of a Vector Version of the 6S Radiative Transfer Code for Atmospheric Correction of Satellite Data. Part I: Path Radiance." *Applied Optics* 45 (26): 6762–6774. <https://doi.org/10.1364/AO.45.006762>.
- Liu, X., and M. Wang. 2020. "Super-Resolution of VIIRS-Measured Ocean Color Products Using Deep Convolutional Neural Network." *IEEE Transactions on Geoscience & Remote Sensing* 59 (1): 114–127. <https://doi.org/10.1109/TGRS.2020.2992912>.
- Luo, Y., D. Doxaran, K. Ruddick, F. Shen, B. Gentili, L. Yan, and H. Huang. 2018. "Saturation of Water Reflectance in Extremely Turbid Media Based on Field Measurements, Satellite Data and Bio-Optical Modelling." *Optics Express* 26 (8): 10435–10451. <https://doi.org/10.1364/OE.26.010435>.
- Luo, Y., D. Doxaran, and Q. Vanhellemont. 2020. "Retrieval and Validation of Water Turbidity at Metre-Scale Using Pléiades Satellite Data: A Case Study in the Gironde Estuary." *Remote Sensing* 12 (6): 946. <https://doi.org/10.3390/rs12060946>.
- Mélin, F., V. Vantrepotte, A. Chuprin, M. Grant, T. Jackson, and S. Sathyendranath. 2017. "Assessing the Fitness-For-Purpose of Satellite Multi-Mission Ocean Color Climate Data Records: A Protocol Applied to OC-CCI Chlorophyll-A Data." *Remote Sensing of Environment* 203:139–151. <https://doi.org/10.1016/j.rse.2017.03.039>.
- Miller, R. L., and B. A. McKee. 2004. "Using MODIS Terra 250 M Imagery to Map Concentrations of Total Suspended Matter in Coastal Waters." *Remote Sensing of Environment* 93 (1–2): 259–266. <https://doi.org/10.1016/j.rse.2004.07.012>.
- Mobley, C. D. 1999. "Estimation of the Remote-Sensing Reflectance from Above-Surface Measurements." *Applied Optics* 38 (36): 7442–7455. <https://doi.org/10.1364/AO.38.007442>.
- Nechad, B., K. G. Ruddick, and G. Neukermans. 2009. "Calibration and Validation of a Generic Multisensor Algorithm for Mapping of Turbidity in Coastal Waters." In *SPIE Europe Remote Sensing, Remote Sensing of the Ocean, Sea Ice, and Large Water Regions*, Berlin, Germany, 74730H. International Society for Optics and Photonics.
- Novoa, S., D. Doxaran, A. Ody, Q. Vanhellemont, V. Lafon, B. Lubac, and P. Gernez. 2017. "Atmospheric Corrections and Multi-Conditional Algorithm for Multi-Sensor Remote Sensing of Suspended Particulate Matter in Low-To-High Turbidity Levels Coastal Waters." *Remote Sensing* 9 (1): 61. <https://doi.org/10.3390/rs9010061>.
- Ody, A., D. Doxaran, Q. Vanhellemont, B. Nechad, S. Novoa, G. Many, F. Bourrin, R. Verney, I. Pairaud, and B. Gentili. 2016. "Potential of High Spatial and Temporal Ocean Color Satellite Data to Study the Dynamics of Suspended Particles in a Micro-Tidal River Plume." *Remote Sensing* 8 (3): 245. <https://doi.org/10.3390/rs8030245>.
- Qi, L., C. Hu, K. Mikelsons, M. Wang, V. Lance, S. Sun, B. B. Barnes, J. Zhao, and D. Van der Zande. 2020. "In Search of Floating Algae and Other Organisms in Global Oceans and Lakes." *Remote Sensing of Environment* 239:111659. <https://doi.org/10.1016/j.rse.2020.111659>.
- Ruddick, K., A. Bialek, V. Ernesto Brando, P. De Vis, A. Ines Dogliotti, D. Doxaran, P. Goryl, et al. 2024. "HYPERNETS: A Network of Automated Hyperspectral Radiometers to Validate Water and Land Surface Reflectance (380–1700 Nm) from All Satellite Missions." *Frontiers in Remote Sensing* 5:1372085. <https://doi.org/10.3389/frsen.2024.1372085>.

- Ruddick, K. G., V. De Cauwer, Y.-J. Park, and G. Moore. 2006. "Seaborne Measurements of Near Infrared Water-Leaving Reflectance: The Similarity Spectrum for Turbid Waters." *Limnology & Oceanography* 51 (2): 1167–1179. <https://doi.org/10.4319/lo.2006.51.2.1167>.
- Sathyendranath, S., R. J. W. Brewin, C. Brockmann, V. Brotas, B. Calton, A. Chuprin, P. Cipollini, et al. 2019. "An Ocean-Colour Time Series for Use in Climate Studies: The Experience of the Ocean-Colour Climate Change Initiative (OC-CCI)." *Sensors* 19 (19): 4285. <https://doi.org/10.3390/s19194285>.
- Vandermeulen, R. A., R. Arnone, S. Ladner, and P. Martinolich. 2015. "Enhanced Satellite Remote Sensing of Coastal Waters Using Spatially Improved Bio-Optical Products from SNPP-VIIRS." *Remote Sensing of Environment* 165:53–63. <https://doi.org/10.1016/j.rse.2015.04.026>.
- Vanhellemont, Q. 2019. "Adaptation of the Dark Spectrum Fitting Atmospheric Correction for Aquatic Applications of the Landsat and Sentinel-2 Archives." *Remote Sensing of Environment* 225:175–192. <https://doi.org/10.1016/j.rse.2019.03.010>.
- Vanhellemont, Q. 2020. "Sensitivity Analysis of the Dark Spectrum Fitting Atmospheric Correction for Metre-And Decametre-Scale Satellite Imagery Using Autonomous Hyperspectral Radiometry." *Optics Express* 28 (20): 29948–29965. <https://doi.org/10.1364/OE.397456>.
- Vanhellemont, Q. 2023. "Evaluation of Eight Band SuperDove Imagery for Aquatic Applications." *Optics Express* 31 (9): 13851–13874. <https://doi.org/10.1364/OE.483418>.
- Vanhellemont, Q., and K. Ruddick. 2018. "Atmospheric Correction of Metre-Scale Optical Satellite Data for Inland and Coastal Water Applications." *Remote Sensing of Environment* 216:586–597. <https://doi.org/10.1016/j.rse.2018.07.015>.
- Vanhellemont, Q., and K. Ruddick. 2021. "Atmospheric Correction of Sentinel-3/OLCI Data for Mapping of Suspended Particulate Matter and Chlorophyll-A Concentration in Belgian Turbid Coastal Waters." *Remote Sensing of Environment* 256:112284. <https://doi.org/10.1016/j.rse.2021.112284>.
- Vansteewegen, D., K. Ruddick, A. Cattrijsse, Q. Vanhellemont, and M. Beck. 2019. "The Pan-And-Tilt Hyperspectral Radiometer System (PANTHYR) for Autonomous Satellite Validation Measurements —Prototype Design and Testing." *Remote Sensing* 11 (11): 1360. <https://doi.org/10.3390/rs11111360>.
- Vansteewegen, D., and Q. Vanhellemont. 2023. "PANTHYR Hyperspectral Water Reflectance - O1BE." <https://doi.org/10.5281/zenodo.10024143>.
- Wang, M., and L. Jiang. 2018. "VIIRS-Derived Ocean Color Product Using the Imaging Bands." *Remote Sensing of Environment* 206:275–286. <https://doi.org/10.1016/j.rse.2017.12.042>.
- Wolfe, R. E., G. Lin, M. Nishihama, K. P. Tewari, J. C. Tilton, and A. R. Isaacman. 2013. "Suomi NPP VIIRS Prelaunch and On-Orbit Geometric Calibration and Characterization." *Journal of Geophysical Research Atmospheres* 118 (20): 11–508. <https://doi.org/10.1002/jgrd.50873>.